ScienceDaily
Your source for the latest research news

Large parts of Europe are warming twice as fast as the planet on average

Date: November 22, 2022

Source: Stockholm University

Summary: The warming during the summer months in Europe has been much faster than the global average, shows a new study. As a consequence of human emissions of greenhouse gases, the climate across the continent has also become drier, particularly in southern Europe, leading to worse heat waves and an increased risk of fires.

FULL STORY

The warming during the summer months in Europe has been much faster than the global average, shows a new study by researchers at Stockholm University published in the *Journal of Geophysical Research Atmospheres*. As a consequence of human emissions of greenhouse gases, the climate across the continent has also become drier, particularly in southern Europe, leading to worse heat waves and an increased risk of fires.

According to the UN's Intergovernmental Panel on Climate Change (IPCC), warming over land areas occurs significantly faster than over oceans, with 1.6 degrees and 0.9 degrees on average, respectively. It means that the global greenhouse gas emissions budget to stay under a 1.5-degree warming on land has already been used up. Now, the new study shows that the emissions budget to avoid a 2-degree warming over large parts of Europe during the summer half-year (April-September) has also been used up. In fact, measurements reveal that the warming during the summer months in large parts of Europe during the last four decades has already surpassed two degrees.

"Climate change is serious as it leads to, among other things, more frequent heat waves in Europe. These, in turn, increase the risk of fires, such as the devastating fires in southern Europe in the summer of 2022," says Paul Glantz, Associate Professor at the Department of Environmental Science, Stockholm University, and main author of the study.

In southern Europe, a clear, so-called, positive feedback caused by global warming is evident, i.e. warming is amplified due to drier soil and decreased evaporation. Moreover, there has been less cloud coverage over large parts of Europe, probably as a result of less water vapour in the air.

"What we see in southern Europe is in line what IPCC has predicted, which is that an increased human impact on the greenhouse effect would lead to dry areas on Earth becoming even drier," says Paul Glantz.

Impact of aerosol particles

The study also includes a section about the estimated impact of aerosol particles on the temperature increase. According to Paul Glantz, the rapid warming in, for example, Central and Eastern Europe, is first and foremost a consequence of the human emissions of long-lived greenhouse gases, such as carbon dioxide. But since emissions of short-lived aerosol particles from, for example, coal-fired power plants have decreased greatly over the past four decades, the combined effect has led to an extreme temperature increase of over two degrees.

"The airborne aerosol particles, before they began to decrease in the early 1980s in Europe, have masked the warming caused by human greenhouse gases by just over one degree on average for the summer half-year. As the aerosols in the atmosphere decreased, the temperature increased rapidly. Human emissions of carbon dioxide are still the biggest threat as they affect the climate for hundreds to thousands of years," says Paul Glantz.

According to Paul Glantz, this effect provides a harbinger of future warming in areas where aerosol emissions are high, such as in India and China.

Background facts -- The greenhouse effect and aerosol effect

Fossil burning leads to the release of both aerosol particles and greenhouse gases. Although their source is common, their effects on climate differ.

About the greenhouse effect

Greenhouse gases are largely unaffected by solar radiation while they absorb infrared radiation efficiently, leading to re-emission towards the Earth's surface. The Earth absorbs both solar radiation and infrared radiation, which leads to the warming of the lower part of the atmosphere in particular.

Time-space: Greenhouse gases are generally long-lived in the atmosphere and this applies above all to carbon dioxide where human emissions affect climate for hundreds to thousands of years. It also means that greenhouse gases spread evenly over the entire planet.

About the aerosol effect

In contrast to greenhouse gases, aerosol particles affect incoming solar radiation, i.e. they scatter part of the sunlight back into space causing a cooling effect. Human emissions of aerosols can enhance this cooling effect.

Time-space: Airborne human aerosol particles have a lifetime of about a week, which means that they mainly cool the climate locally or regionally and in the short term.

According to the Paris Agreement, all parties must commit to drastically reduce their greenhouse gas emissions, but it is also important to decrease concentrations of aerosol particles as well because, in addition to their effects on climate, aerosol particles in polluted air cause approximately eight million premature deaths each year around the world.

Story Source:

Materials provided by **Stockholm University**. *Note: Content may be edited for style and length.*

Journal Reference:

1. P. Glantz, O. G. Fawole, J. Ström, M. Wild, K. J. Noone. **Unmasking the Effects of Aerosols on Greenhouse Warming Over Europe**. *Journal of Geophysical Research: Atmospheres*, 2022; 127 (22) DOI: 10.1029/2021JD035889

Cite This Page:

MLA APA Chicago

Stockholm University. "Large parts of Europe are warming twice as fast as the planet on average." ScienceDaily. ScienceDaily, 22 November 2022. <www.sciencedaily.com/releases/2022/11/221122111407.htm>.

ADVANCING EARTH AND SPACE SCIENCE

JGR Atmospheres

RESEARCH ARTICLE

10.1029/2021JD035889

Unmasking the Effects of Aerosols on Greenhouse Warming Over Europe

P. Glantz[1], O. G. Fawole[1,2], J. Ström[1], M. Wild[3], and K. J. Noone[1]

[1]Department of Environmental Science, Stockholm University, Stockholm, Sweden, [2]Department of Physics and Engineering Physics, Obafemi Awolowo University, Ile-Ife, Nigeria, [3]Institute for Atmospheric and Climate Science, ETH Zurich, Zurich, Switzerland

Key Points:

- Substantial increase in near surface temperature was found during decline in aerosols for Central and Eastern Europe
- Total warming for clear-sky summer conditions over large parts of Europe since 1979 is nearly double the global mean temperature record
- Rapid warming over Iberian Peninsula is likely caused by enhanced greenhouse effect, dryer surfaces, and to some degree decline in aerosols

Correspondence to:

P. Glantz,
paul.glantz@aces.su.se

Citation:

Glantz, P., Fawole, O. G., Ström, J., Wild, M., & Noone, K. J. (2022). Unmasking the effects of aerosols on greenhouse warming over Europe. *Journal of Geophysical Research: Atmospheres*, *127*, e2021JD035889. https://doi.org/10.1029/2021JD035889

Received 17 SEP 2021
Accepted 28 OCT 2022

Author Contributions:

Conceptualization: J. Ström
Data curation: O. G. Fawole, M. Wild
Formal analysis: J. Ström, M. Wild
Methodology: J. Ström, M. Wild, K. J. Noone
Resources: J. Ström
Validation: M. Wild
Writing – original draft: O. G. Fawole
Writing – review & editing: O. G. Fawole, J. Ström, K. J. Noone

Abstract

Aerosol optical thickness (AOT) has decreased substantially in Europe in the summer half year (April–September) since 1980, with almost a 50% reduction in Central and Eastern Europe, according to Modern-Era Retrospective analysis for Research and Applications, Version 2 (MERRA-2) reanalysis. At the same time, strong positive trends in ERA5 reanalysis surface solar radiation downward for all-sky and clear-sky conditions (SSRD and SSRDc, respectively) and temperature at 2 m are found for Europe in summer during the period 1979–2020. The GEBA observations show as well strong increases in SSRD during the latest four decades. Estimations of changes in SSRDc, using the Santa Barbara DISORT Atmospheric Radiative Transfer (SBDART) model, show similarly strong increases when fed by MERRA-2 AOT. The estimates of warming in this study, caused by increases in SSRD and SSRDc, are based on energy budget approximations and the Stefan Boltzmann law. The increases in near surface temperature, estimated both for clear-sky and all-sky conditions, are up to about 1°C for Central and Eastern Europe. The total warming over large parts of this region for clear-sky conditions is however nearly double the global mean temperature increase of 1.1°C, while somewhat less for all-sky conditions. The effects of aerosols on warming over the southerly Iberian Peninsula are weaker compared to countries further north. The rapid total warming over the Iberian Peninsula is probably caused by greenhouse warming, drier surface conditions, and to some degree decline in aerosols. Reduced cloud cover is found for large parts of Europe in summer during the latest four decades.

Plain Language Summary

Aerosol particles cool the planet, but this effect is short-lived in comparison with human impact on the greenhouse effect. This study shows that the greatest cooling effect in Europe has taken place in Central and Eastern Europe over the past four decades. The average temperature for the period April–September has increased by around 1°C due to reduced levels of aerosol particles. This is relevant for other areas of the Earth where the levels of aerosol particles are elevated today. This means that aerosol particles mask future warming if emissions begin to decrease, for example, in Eastern China and India. The total warming over large parts of Europe is however twice as large, and then also to the global average temperature increase of about 1.1°C. Positive feedbacks, by way of dryer surface conditions and reduced cloud cover, due to enhanced greenhouse effect have highly contributed to the rapid warming observed. Human emissions of carbon dioxide are the major threat, as the greenhouse gase affects the climate for hundreds to thousands of years.

1. Introduction

An energy balance for the Earth is established when incoming solar energy absorbed by the planet (Earth-atmosphere system) is balanced by an equal amount of reflected solar radiation and emitted thermal infrared radiation (Liou, 2002). The Earth's climate system is however perturbed (SPM A.1.2 in IPCC, 2021); global surface mean temperature was 1.09°C (0.95–1.20)°C higher in 2011–2020 than 1850–1900, with larger increases over land (1.59°C [1.34–1.83]°C) than over the oceans (0.88°C [0.68–1.01]°C). This is mainly attributed to an enhanced greenhouse effect, with more of infrared radiation being trapped by anthropogenic greenhouse gases (GHGs, e.g., IPCC, 2014, 2021; Lashof & Ahuja, 1990; Svensen et al., 2007). Some regions on Earth, for example, the Arctic, have experienced a much faster warming (Cohen et al., 2014; Maturilli et al., 2014; Serreze & Barry, 2011). Like the rest of the Mediterranean region, the Iberian Peninsula is as well very sensitive and vulnerable to the ongoing global warming (Christensen et al., 2013; Gago et al., 2011; Giorgi, 2006). Abundant evidence indicates that the subtropical climate zone has shifted toward higher latitudes under climate change (Archer & Caldeira, 2008; Fu et al., 2006; Hu et al., 2013, 2018; Johanson & Fu, 2009; Seidel et al., 2008; H. Yang et al., 2020). Christidis and Stott (2021) applied an ensemble of new climate models and compared experiments with and without the effect of human influence to assess the anthropogenic contribution for Europe. The results indicate summertime widespread drier conditions for the last decades, which are more extreme in Southern Europe. In addition, Tuel and Eltahir (2021) analyzed observations and output from models from Phase 5 of the Coupled Model Intercomparison Project (CMIP5) and found that winter precipitation declines, consequently depleting soil moisture in Southern Europe during spring, which also results in drier summers due to soil moisture–precipitation feedbacks. Furthermore, it is estimated that at 1.5°C warming, about 14% of the Earth's population will be exposed to severe heat waves at least once every 5 years, and this could rise to 37% at 2°C warming (Section 3.3.2 in IPCC, 2022). During the period 1980–2005, the frequency, intensity, and duration of extremely hot days (heat waves) have been found to be higher in Europe compared to Eastern US and Eastern Asia (Luo et al., 2020). Lorenz et al. (2019) reported that on average across Europe, the number of days with extreme heat and heat stress has more than tripled and hot extremes have warmed by 2.3°C from 1950 to 2018. They also found that over Central Europe, the warming exceeds the corresponding summer mean warming by 50%.

Beside emissions of GHG, anthropogenic activities result in a varying level and types of coemitted aerosols and their gaseous precursors. Since preindustrial times, the level of these shave increased significantly (Granier et al., 2011; Lamarque et al., 2010; Smith et al., 2011). Atmospheric aerosols play an important role in the perturbation of the Earth's radiation balance, both directly and indirectly (IPCC, 2013, 2021; Yi et al., 2012). Depending on their physical, chemical, and optical properties, the interaction of aerosols with incoming solar radiation in the cloud-free atmosphere results in either cooling or warming (Seinfeld & Pandis, 2016). While for example, anthropogenic sulfates and nitrates scatter solar radiation back to space (cooling the surface), black and brown carbon absorb solar radiation, and consequently have a warming effect in the lower troposphere. The impact of aerosols on the Earth-atmosphere energy budget is associated with large uncertainties (Boucher & Haywood, 2001; IPCC, 2014, 2021), particularly due to complex interactions of aerosols with clouds (indirect aerosol effect). Even so, second to GHGs, man-made aerosols have caused the largest anthropogenic radiative forcing (with opposite sign) during the industrial era (Boucher et al., 2013; IPCC, 2021). The global effective radiative forcing of CO_2 has however increased substantially since 1980, while relatively small changes are found in the global effective radiative forcing of the aerosols (Figure TS9d in IPCC, 2021).

Air quality mitigation in Europe and North America since the early 1980s has led to regional reductions in anthropogenic emissions (Hand et al., 2012; Smith et al., 2011; Vestreng et al., 2007). Emissions of SO_2 have been reduced by 73% in Europe during the period 1980–2004 (Vestreng et al., 2007). Based on model simulations, Turnock et al. (2016) estimated that European emissions of sulfur dioxide, black carbon, and organic carbon have been reduced by 53%, 59%, and 32%, respectively, between 1970 and 2010. This in turn has resulted in a significant reduction of boundary layer aerosols in European cities (e.g., Turnock et al., 2015, 2016). Based on particle matter ($PM_{2.5}$) measurements from European Monitoring and Evaluation Programme (EMEP), Mortier et al. (2020) reported significant negative trends in Europe between 2000 and 2014. In addition, at the rural background site Aspvreten, Southern Sweden, Tunved and Ström (2019) found decreased aerosol mass and number concentrations during the period 2000–2017.

The aggregate of direct and diffuse radiation reaching the Earth surface for all-sky conditions is termed surface solar radiation downward (SSRD). Changes in SSRD have great implications for plant physiology and yields, the Earth's hydrological processes, air quality and human health, and climate (Jong & Stewart, 1993; Ramanathan et al., 2001; Wang et al., 2020). Global "dimming" and "brightening" are terms describing significant decadal changes in the amount of SSRD (Pinker et al., 2005; Stanhill & Cohen, 2001; Wild, 2009; Wild et al., 2021). As a result of reduced aerosol and precursor emissions in North America and Europe, positive trends in SSRD have been observed from the early 1980s (Wild et al., 2005). Changes in SSRD can be attributed to factors including variation in aerosol loading (Kim & Ramanathan, 2008; Xia et al., 2006), cloud cover (Wang & Yang, 2014), cloud feedbacks (Liepert, 2002), and aerosol–cloud interactions (Kaufman et al., 2005). Based on a long-term observational radiation record (1947–2017) at Potsdam, Germany, Wild et al. (2021) found multidecadal variations in surface solar radiation on the order of 10 W m^{-2} that was attributed first to dimming and thereafter brightening caused mainly by anthropogenic aerosols. Furthermore, Wang et al. (2020) established that some properties of atmospheric aerosols, such as aerosol optical thickness (AOT) and single scattering albedo, have significant implications on trends in SSRD, both considering local and regional scales. Latitudinal distribution (zonal average) of relative AOT tendencies derived from Level 3 MODerate resolution Imaging Spectroradiometers (MODIS) global monthly AOT for the period 2000–2006 shows negative trends within the range of −5.7%

to about −3% per year at middle and high latitudes in the Northern Hemisphere (Kishcha et al., 2007). AErosol RObotic NETwork (AERONET, Holben et al., 1998) sites across Europe and MODIS (de Meij et al., 2012; Glantz et al., 2019; Mortier et al., 2020; Turnock et al., 2015) have shown decline in AOT in recent decades.

In addition to being influenced by decadal trends in aerosols, SSRD can also be affected by changes in cloud fraction. Sfică et al. (2020) found that changes in atmospheric circulation during the period 1981–2014 were accompanied generally by a reduction of the cloud cover in Europe, with a maximum change over Eastern Europe. Their results relied on five data sets: four reanalysis sets and the fifth based on satellite retrievals from the Advanced Very High-Resolution Radiometers. Blanc et al. (2022) investigated possible changes in large-scale circulation over the period 1950–2019 for Western Europe using European Centre for Medium-range Weather Forecasts (ECMWF, Hersbach et al., 2019) ERA5 reanalysis. They found that anticyclonic conditions tend to become more stationary in summer. For the Iberian Peninsula, Mateos et al. (2014) found that 75% of a positive trend in SSRD, observed between 2003 and 2012, was caused by reductions in clouds, while the remaining 25% was related to decline in aerosols.

Y. Yang et al. (2020) have examined trends in aerosols over Europe for the period 1980–2018 and quantified contributions from 16 source regions using the CAM model. A decrease in sulfate loading led to an increase of 2 W m^{-2} in Europe during this period, with 12% caused by non-European emissions. Considering decreases in all anthropogenic aerosols between 1980 and 2015, a mean net effective radiative forcing of somewhat above 4 W m^{-2} is reported for Europe (Figure 6.11 in Szopa et al., 2021). An analysis of 312 ground-based stations with sunshine duration series, a proxy for global radiation, shows strong positive correlations with near surface temperature in Europe (van den Besselaar et al., 2015). The strongest correlation was found for summer. Based on the NorESM Earth system model, Acosta Navarro et al. (2016) found an increase in annual mean temperature of about 0.4°C, due to decline in sulfate aerosols, for Central Europe over the period 1996–2005. Using energy budget approximations, Turnock et al. (2016) estimated that negative trends in emissions of aerosol precursors in Europe during the period 1970–2010 have caused an increase in annual mean surface temperature near that value: 0.45°C ± 0.11°C. Nabat et al. (2014) used the fully coupled regional climate model CNRM-RCSM4 to demonstrate the impact of sulfate aerosol changes on radiation and temperature. Based on sulfate aerosol decreases included and excluded in two simulations, they found that aerosol reductions have contributed with 23% ± 5% to the warming in Europe over the period 1980–2012. Furthermore, observations indicate rapid increase in summer (June–August) mean surface temperature since the mid-1990s over Western Europe (Dong et al., 2017). A set of experiments using the atmospheric component of the HadGEM3 global climate model were analyzed to understand the causes of the warming. The authors conclude that changes in sea surface temperature/sea ice extent explain 62.2% ± 13.0% of mean warming over Western Europe, while the remaining 37.8% ± 13.6% of the warming is explained directly by changes in anthropogenic GHGs and aerosols. Based on CMIP5, Undorf et al. (2018) reported that anthropogenic aerosols explain more than a third of the simulated interdecadal forced variability of European near surface temperature.

The aim of the present study is to investigate impacts of reduced aerosol loading and cloud cover on the warming in Europe in the summer half year (April–September) over the period 1979–2020. The effects on warm extremes in Europe from both anthropogenic aerosols and GHGs are most relevant during this period of the year. To get a holistic view of climate changes in Europe, results of total warming in Europe, for both clear-sky and all-sky conditions, will be presented as well. In the present study, data from the Modern-Era Retrospective analysis for Research and Applications (MERRA-2, Version 2, Randles et al., 2017) and ERA5 have been investigated. Results of ERA5 surface solar radiation downward for clear-sky conditions (SSRDc) as well as SSRD, low cloud cover (LCC), and total cloud cover (TCC) for all-sky conditions will be presented. Changes in SSRD and SSRDc have been investigated in combination with ERA5 upward surface terrestrial radiation for all-sky and clear-sky conditions separated (STRU and STRUc, respectively). Contributions to changes in near surface temperature likely caused by a reduction in aerosol loading are estimated by comparing the approximate latest decade (2010s: 2009–2020) with the approximate reference decade (1980s: 1979–1989). These estimates are based on energy budget approximations using data sets presented above and the Stefan Boltzmann law. Comparison of the two decades, 1980s and 2010s, for the ERA5 parameters investigated in this study has been obtained for the same years as above, with the exception for SSRDc in the comparison with radiative transfer modeling (Section 2.2).

10.1029/2021JD035889

2. Data and Methodology

2.1. Meteorological and Aerosol Data

2.1.1. ERA5 Meteorological Reanalysis

The reanalysis from ECMWF combines model data with historical satellite and in situ measurements into a globally complete and consistent data set. ERA5 is the fifth generation ECMWF reanalysis for the global climate and weather. Johannsen et al. (2019) have shown a reduction in ERA5 temperature biases compared to older versions of the reanalysis. ERA5 data are available from 1950, subdivided with respect to the periods 1950–1978 (preliminary back extension, Bell et al., 2020) and 1979 onward (final release, Hersbach et al., 2019). The ERA5 full data set from 1950 has been included in this study to better characterize decadal variability. The monthly mean data sets at the surface level used in the present study, averaged for April–September, have a latitude–longitude grid of 0.25° × 0.25° (Dee et al., 2014). The following ERA5 variables have been investigated: temperature at 2 meters (T_{2m}), skin temperature (T_{Skin}), SSRDc, SSRD, total heat flux (HF) that is also separated for surface sensible and latent heat fluxes (SSHF and SLHF, respectively), STRUc and STRU, as well as LCC and TCC. The ERA5 reanalysis implies that meteorological parameters (temperature, pressure, wind, and humidity) are pushed toward observations every few hours using data assimilation. The effect of aerosols on radiative transfer is based on prescribed climatological distributions of optical thickness from sea salt, soil/dust, organic, black carbon, and sulfate. Input are monthly mean geographical fields for optical thickness at the surface from Tegen et al. (1997). The CMIP5 data set, derived from observations, is used in ERA5 for long-term aerosol trends (Hersbach et al., 2015). The radiation calculations use diagnostic fields of temperature, pressure, water vapor, aerosol, and cloud properties, some of which are better constrained by observations than others. The radiation parameters for clear-sky conditions are obtained by calling the radiation scheme twice by setting the cloud amount to zero in the second call.

2.1.2. Global Historical Climatology Network-Monthly Mean Temperature

Global Historical Climatology Network-Monthly (GHCN-M) version 4 data set of monthly mean temperatures was accessed from NOAA's National Centers for Environmental Information (NCEI) database (Lawrimore et al., 2011). NCEI's global land surface homogenized temperature data set provides monthly average temperatures from over 40,000 stations, some of which contain records more than 300 years back in time. This data set is considered to be the most comprehensive suite of global temperature and precipitation observations in the world. Temperature data for April–September of the period 1950–2020 and from 43 stations in France, Germany, Spain, and Ukraine are included in the present results. Information about the stations and investigation are given in Section 3.1 and Table A1.

2.1.3. MERRA-2 AOT Reanalysis

MERRA data are managed by NASA's Global Modeling and Assimilation Office (GMAO). GMAO aimed to place historical observations from NASA's Earth Observing System satellites into the Goddard Earth Observing System (GEOS) atmospheric modeling and data assimilation system (Rienecker et al., 2011). MERRA-2, the second version of MERRA, is the latest generation of the reanalysis, which addresses the limitations of the first version with the updated Earth system model of GEOS, version 5 (GEOS-5). MERRA-2 is the first long-term global reanalysis to assimilate space-based observations of aerosols and represent their interactions with other physical processes in the climate system. An advanced Atmosphere Data Assimilation System is adopted for aerosol observation in MERRA-2 (Randles et al., 2017). Aerosol and meteorological observations are assimilated within GEOS-5 with very careful cloud screening and homogenization of the observing system by means of a net scheme that translates MODIS and space-based Advanced Very High-Resolution Radiometer radiances into AERONET calibrated AOT (Buchard et al., 2017). The MERRA-2 AOT at the 550 nm wavelength included in this study is obtained from a high-resolution reanalysis data set (0.5° × 0.625° latitude-by-longitude grid, ca. 50 km in the latitudinal direction, 72 model layers up to 0.01 hPa). The MERRA-2 reanalysis covers the period from 1 January 1980 to within a couple weeks of real time.

2.1.4. AERONET Sun Photometer Measurements

MERRA-2 monthly AOTs at 550 nm have been validated against AERONET (version 3) level 2.0 data (quality assured) from eight stations in Europe (Table 1). Information about the CIMEL sun photometers operated at these sites can be found at http://aeronet.gsfc.nasa.gov. These values were recorded every 15 min and automatically

Table 1
AERONET AOT Measurements and Comparison of Trend (ΔAOT [Year^{-1}])

Site	Lat./long.	Altitude (m)	Country	Period[a]	$\Delta AOT_{AERONET}$[b]	ΔAOT_{MERRA2}[c]
Belsk	51.8°N, 20.8°E	190	Poland	2004–2020	−0.0014 (88%)	−0.0017
						−0.0026
Birkness	58.4°N, 8.3°E	230	Norway	2009–2020	−0.0005 (86%)	0.0006
						−0.0007
Brussels	50.8°N, 4.4°E	120	Belgium	2006–2020	−0.0064 (86%)	−0.0006
						−0.0017
Chilboltonn	51.1°N, 1.4°W	88 m	United Kingdom	2005–2019	−0.0044 (87%)	−0.0004
						−0.0015
Evora	38.6°N, 7.9°E	293	Portugal	2010–2020	−0.0002 (100%)	0.0001
						−0.0004
Granada	37.2°N, 3.6°E	680	Spain	2005–2020	−0.0029 (84%)	−0.0010
						−0.0011
Gustav Dalen	58.6°N, 17.5°E	25	Sweden	2005–2020	−0.0011 (75%)	0.0010
						−0.0004
Kuopio	62.9°N, 27.6°E	105	Finland	2008–2020	−0.0017 (96%)	0.0002
						−0.0012
Mainz	50.0°N, 8.3°E	150	Germany	2003–2020	−0.0037 (82%)	−0.0012
						−0.0020
Moldova	47.0°N, 28.8°E	205	Moldova	1999–2018	−0.0053 (78%)	−0.0042
						−0.0039
Palaiseau	48.8°N, 2.2°E	156	France	1999–2020	−0.0048 (53%)	−0.0014
						−0.0014
Toravere	58.3°N, 26.5°E	85	Estonia	2002–2020	−0.0026 (97%)	−0.0014
						−0.0019

[a]April–September. [b]In parentheses, number of months (in percent) included in the comparison. [c]The first and second trend values are obtained for the same years as AERONET (column 5) and the period 1999–2020, respectively.

cloud screened (Smirnov et al., 2000). AERONET-derived estimates of spectral AOT are expected to be accurate within <±0.01 for wavelengths longer than 440 nm (e.g., Holben et al., 1998). Since AERONET does not provide AOT at the wavelength 550 nm, it has been estimated from three wavelengths within 440–675 nm. The expressions of the regression coefficient (Ångström exponent), regression constant, and interpolation of AOT at 550 nm are described in Section 2.5.

2.1.5. Global Energy Balance Archive SSRD Measurements

The Global Energy Balance Archive (GEBA) is a database for central storage of the worldwide energy flux measurements at the Earth's surface, maintained at ETH Zurich, Switzerland (Wild et al., 2017). GEBA contains in its 2017-version around 500,000 monthly mean entries of various surface energy balance components measured at 2,500 locations. The GEBA database contains observations from 15 surface energy flux components, with the most widely measured quantity being SSRD. Many of the historic records extend over several decades and monthly data from 29 ground-based stations in countries corresponding to Eastern Europe, Germany, France, and Iberian Peninsula (Table A2) have been included in the validation of ERA5 SSRD.

2.2. Santa Barbara DISORT Atmospheric Radiative Transfer SSRDc Calculations for Clear-Sky Conditions

The Santa Barbara DISORT Atmospheric Radiative Transfer (SBDART) model relies on LOWTRAN-7 atmospheric transmission calculations and the radiative transfer equation is numerically integrated with the DISORT radiative transfer module (Ricchiazzi et al., 1998). The model was developed at the University of California, Santa Barbara, USA. The main inputs used in SBDART estimations are MERRA-2 AOT at 550 nm, ozone concentration obtained from https://giovanni.gsfc.nasa.gov/giovanni/, and atmospheric concentration of trace gases CH_4, N_2O, and CO_2 from the Earth System Research Laboratory (ESRL) Global Monitoring Laboratory database (https://www.esrl.noaa.gov/gmd/dv/data/). The solar zenith angle was calculated using a built-in code in the model by giving the date (month and day), time, and coordinates (longitude and latitude). The latter corresponding to the ground-based stations in Figure 1, with information in Table A1. Clear-Sky SSRDc estimates by the SBDART model, averaged with respect to April–September and each of the decades 1980s (1980–1989), 1990s (1990–1999), 2000s (2000–2009), and 2010s (2010–2019), have been compared with ERA5 SSRDc.

2.3. Method to Estimate Changes in Temperature Caused by Increases in SSRDc and STRD

Estimates of changes in near surface temperature in Europe (on pixel basis and for different areas in Europe), separately for all-sky and clear-sky conditions, are derived from increases in incoming solar radiation by comparing decadal means for 1980s and 2010s with respect to April–September. Not all the extra energy from the difference between 2010 and 1980, represented by ΔSSRD and ΔSSRDc for all-sky and clear-sky conditions, respectively, are directly available to be converted to temperature. As a first step, the enhanced incoming solar radiation must be adjusted ($\Delta SSRD^{adj}$) for the albedo effect and the energy that is converted to energy fluxes other than terrestrial radiation near the surface. The albedo effect is obtained from surface solar radiation upward ($SSRU^{1980s}$), averaged for the 1980s, divided by $SSRD^{1980s}$. Energy fluxes are simply referred to as HF and can be regarded as mainly sensible and latent heat fluxes. The present estimates represent mean conditions for the summer half year and therefore we assume that heat flux to the Earth's crust is small in comparison. Of the potentially available extra solar energy, a fraction is reflected away from the surface, and of the remaining energy a fraction is used to HF. This fraction is defined as HF divided by surface net solar radiation (SNSR). Hence, ΔSSRD and ΔSSRDc are adjusted for albedo and HF according to Equation 1.

$$\Delta \mathrm{SSRD}^{\mathrm{adj}} = \left(\mathrm{SSRD}^{2010\mathrm{s}} - \mathrm{SSRD}^{1980\mathrm{s}}\right) \times \left(1 - \mathrm{SSRU}^{1980\mathrm{s}}/\mathrm{SSRD}^{1980\mathrm{s}}\right) \times \left(1 - \mathrm{HF}^{1980\mathrm{s}}/\mathrm{SNSR}^{1980\mathrm{s}}\right) \quad (1)$$

The first term on the right is the net change in incoming solar radiation. The second and third terms represent adjustment for the albedo effect and energy converted to HF, respectively. The albedo and HF are also site specific. In the all-sky cases, HF is available from the ERA5 data set. For the clear-sky cases, HF has been calculated as the residual from all radiation fluxes in order to reach energy balance at a particular region or pixel. The second step is to calculate the change in temperature from the adjusted SSRD values, using the Stefan Boltzmann law. Emissivity (ε) is not available in the ERA5 data sets, but by using Equation 2 and available data on STRU and T_{Skin} for continental Europe with respect to the 1980s give a mean value with corresponding one standard deviation of 0.999 ± 0.002. For simplicity, a constant value of one was used for ε in this study. The T_{Skin} parameter represents the reference temperature ($T_{\mathrm{Skin}}^{1980\mathrm{s}}$) in the estimation of warming for the all-sky situation and σ is the Stefan Boltzmann constant. The reference temperature for clear-sky conditions is obtained with Stefan Boltzmann law applied on STRUc averaged according to the 1980s. To estimate increases in near surface temperature (shown for the all-sky situation [ΔT_{SSRD}] in Equation 3), indirectly caused by reduced aerosol loading, the Stefan Boltzmann law has been applied on the $\Delta SSRD^{adj}$, by comparing decadal means of the 1980s and 2010s, plus $STRU^{1980s}$ averaged according to the 1980s. In addition, changes in total warming for clear-sky conditions ($\Delta T_{\mathrm{STRUc}}$) are based on Stefan Boltzmann law applied on ΔSTRUc. Changes in $T_{2\mathrm{m}}$ give indication of total warming for the all-sky situation.

$$\mathrm{STRU} = \sigma\, \varepsilon\, T_{\mathrm{Skin}}^{4} \quad (2)$$

$$\Delta T_{\mathrm{SSRD}} = \left(\left(\Delta \mathrm{SSRD}^{\mathrm{adj}} + \mathrm{STRU}^{1980\mathrm{s}}\right)/(\sigma * \varepsilon)\right)^{0.25} - T_{\mathrm{Skin}}^{1980\mathrm{s}} \quad (3)$$

Journal of Geophysical Research: Atmospheres

10.1029/2021JD035889

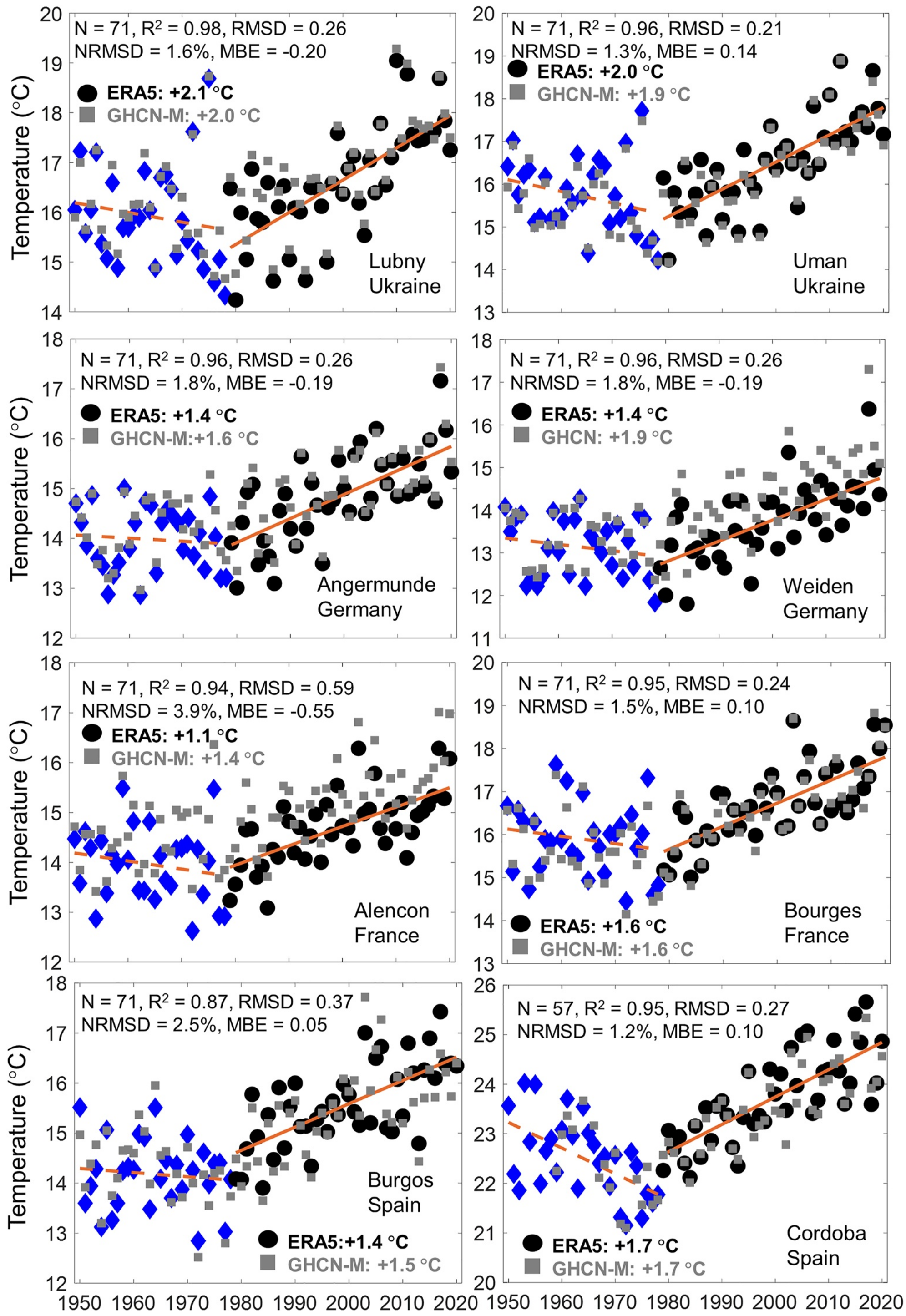

Figure 1. Comparison between ERA5 2-m temperature (T_{2m}) and Global Historical Climatology Network-Monthly (GHCN-M) in situ surface temperature measurements (gray squares) with respect to April–September for eight stations. The blue diamonds and black circles represent ERA5 T_{2m} for the periods 1950–1978 (preliminary version) and 1979–2020 (final release), respectively. The orange lines represent linear fits with respect to ERA5 T_{2m} for the two periods. N is number of months included in the comparison, R^2 is coefficient of determination, RMSD is root mean squared deviation, NRMSD is normalized RMSD, and MBE is mean bias error. Increases in mean temperature (positive values) for ERA5 and GHCN-M are obtained by comparing decadal means for 1980s and 2010s. Information about the sites are given in Table A1.

2.4. Statistical Analysis

Statistical indicators used in these analyses are defined as

$$\mathrm{RMSD} = \left[\frac{1}{n}\sum\nolimits_{i=1}^{n}(y_i - x_i)^2\right]^{1/2} \tag{4}$$

$$\mathrm{NRMSD} = \frac{\mathrm{RMSD}}{\mathrm{meanX}} \tag{5}$$

$$R^2 = 1 - \frac{\mathrm{SS_{res}}}{\mathrm{SS_{tot}}} \tag{6}$$

$$\mathrm{MBE} = \frac{1}{N}\sum\nolimits_{i=1}^{n}(y_i - x_i) \tag{7}$$

where RMSD is the root mean square deviation, NRMSD is the normalized RMSD, R^2 is the coefficient of determination, $\mathrm{SS_{res}}$ and $\mathrm{SS_{tot}}$ are the residual sum of squares and total sum of squares, respectively, MBE is the mean bias error, y_i and x_i represent MERRA-2/ERA5 and AERONET/GHCN-M/GEBA data, respectively, and meanX is mean x_i.

2.5. Deriving AERONET AOT at MERRA-2 Wavelength 550 nm

AERONET AOT (denoted with τ in the equations below) at the wavelengths 440, 500, and 675 nm were used to calculate a least squares logarithmic regression fit to the data (von Hoyningen-Huene et al., 2011). These channels are suitable to derive AERONET AOT at the MERRA-2 wavelength 550 nm and to avoid water vapor absorption (Eck et al., 1999). The spectral slope (denoted with α in Equation 8) and offset β (Equation 9) of the regression line are the Ångström exponent and turbidity coefficient (Ångström, 1929), respectively. Interpolation of AOT at 550 nm is carried out with the Ångström power law (Equation 10). N is the number of the spectral channels used and averaged logarithms of τ and λ are defined as $\overline{\ln\tau} = \frac{1}{N}\sum_{i=1}^{N}\ln\tau(\lambda_i)$ and $\overline{\ln\tau} = \frac{1}{N}\sum_{i=1}^{N}\ln\lambda_i$.

$$\alpha = \frac{\sum_{i=1}^{N}\left[\left(\ln\tau(\lambda_i) - \overline{\ln\tau}\right)\cdot\left(\ln\lambda_i - \overline{\ln\lambda}\right)\right]}{\sum_{i=1}^{N}\left[\ln\lambda_i - \overline{\ln\lambda}\right]^2} \tag{8}$$

$$\beta = \exp\left(\overline{\ln\tau} + \alpha\overline{\ln\lambda}\right) \tag{9}$$

$$\tau_{\lambda=550\mathrm{nm}} = \beta\cdot\lambda^{-\alpha} \tag{10}$$

3. Results

3.1. Trends in ERA5 Surface Temperature

Figure 1 shows changes in mean near surface temperature over the period 1950–2020, averaged with respect to April–September, for eight ground-based stations in Europe. ERA5 mean T_{2m} are validated against GHCN-M in situ temperature measurements from 43 ground-based-stations. Figure 2 (left panel) and Table 2 show the corresponding regional mean results for Ukraine, Germany, France, and Spain. Information about the sites are given in Table A1. Figures 1 and 2 as well as Table 2 show that ERA5 T_{2m} agree reasonably well with GHCN-M temperature measurements, with for example, NRMSD values for the four countries in the range 3.1%–5.3%. ERA5 has a negative bias relative to GHCN-M over all four countries and largest deviation in positive trend, according to the period 1979–2020, is found for Germany (Table 2). Furthermore, the right panel in Figure 2 shows changes in ERA5 T_{STRUc} for clear-sky conditions, derived from STRUc using the Stefan Boltzmann law, for the 43 ground-based stations. Positive trends in temperature from 1979 to 2020 that are statistically significant at the 95% confidence level (F test) are found for both data sources and all stations. Positive values in Figures 1 and 2 (quoted in the legends) denote increases in mean temperature between the 1980s and 2010s. Five ground-based stations located at or near the coast of Spain (Table A1) are not included in the validation. This is because ERA5

10.1029/2021JD035889

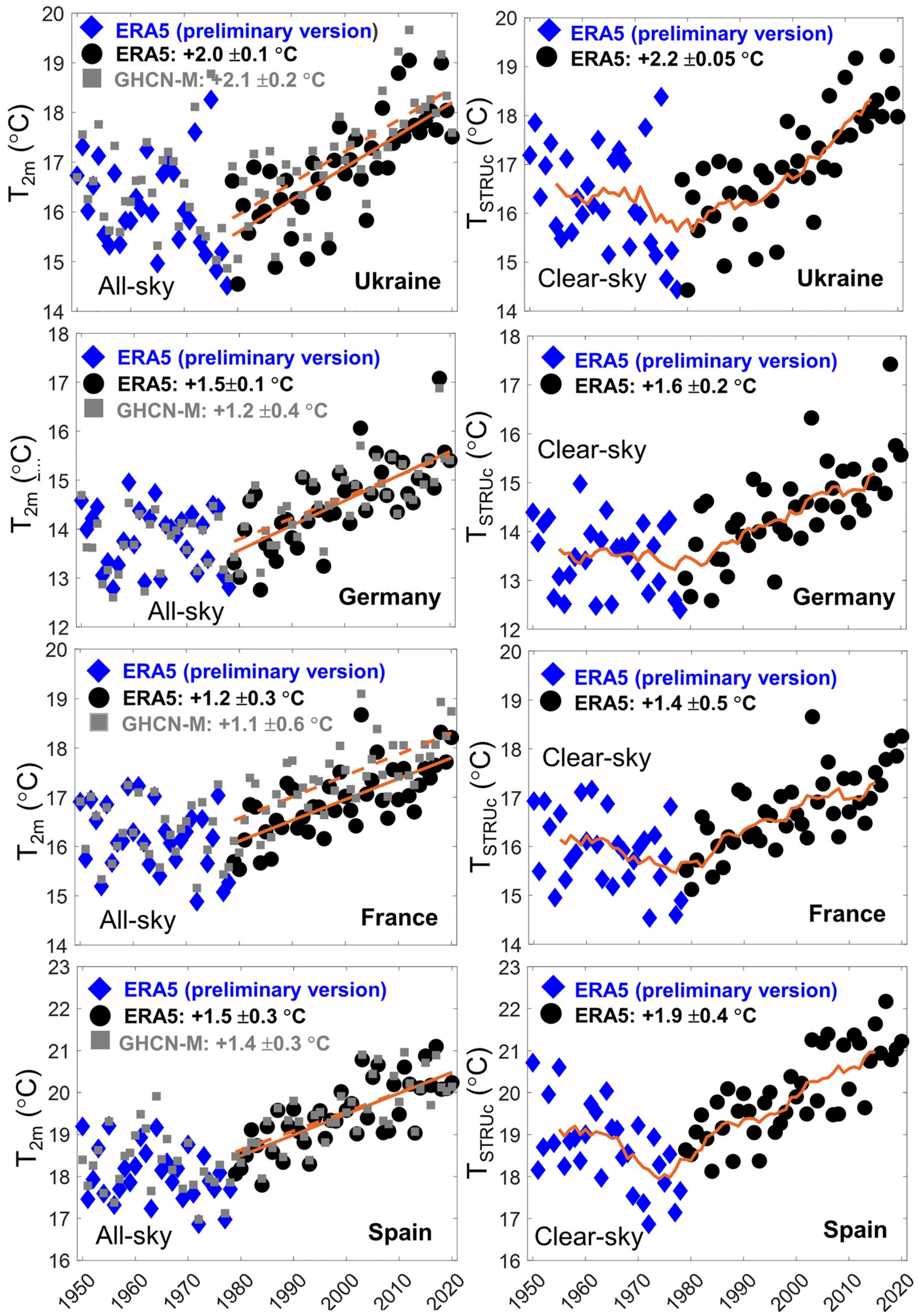

Figure 2. (left) Comparison between ERA5 2-m temperature (T_{2m}) and Global Historical Climatology Network-Monthly (GHCN-M) in situ surface temperature measurements (gray squares) with respect to April–September, all-sky conditions, and four countries. The blue diamonds and black circles represent ERA5 mean T_{2m} for the periods 1950–1978 (preliminary version) and 1979–2020 (final release), respectively. The orange solid and dashed lines represent linear fits for the second period, with respect to ERA5 and GHCN-M temperature values, respectively. Information about the 43 sites included in the comparisons and results of statistical analysis are given in Tables 2 and A1. (right) Changes in ERA5 mean temperature derived from surface terrestrial radiation upward for clear-sky conditions (STRUc) applied on Stefan Boltzmann law (Equation 2) and for the same sites as the left figures. Orange solid line denote 10-year running mean in regards to the ERA5 mean values. (both) Increases in mean temperature (positive values) with corresponding one standard deviation are obtained by comparing decadal means for 1980s and 2010s.

Table 2
Comparison Between ERA5 and GHCN-M Mean Temperature (T) and Trend (ΔT) for the Periods 1950–2020 and 1979–2020, Respectively (April–September)

Country	N_{sites} [a]	N_{all} [b]	R^2	RMSD (°C)	NRMSD (%)	MBE (°C)	T^{GHCN-M} (°C)	T^{ERA5} (°C)	ΔT^{GHCN-M} (°C/year)	ΔT^{ERA5} (°C/year)
Ukraine	5	334 (93%)	0.72	0.89	5.3	−0.29	16.9 ± 1.3	16.6 ± 1.6	0.062 ± 0.004	0.065 ± 0.002
Germany	16	1,058 (96%)	0.59	0.78	5.5	−0.11	14.3 ± 1.1	14.2 ± 1.1	0.042 ± 0.012	0.050 ± 0.004
France	9	639 (100%)	0.96	0.55	3.2	−0.34	17.0 ± 2.1	16.6 ± 1.9	0.043 ± 0.012	0.042 ± 0.012
Spain	13	891 (97%)	0.91	0.89	4.7	−0.20	19.0 ± 2.9	18.8 ± 2.9	0.047 ± 0.011	0.050 ± 0.009

[a]Number of sites included in the estimates of trend (1979–2020). [b]Number of compared values for R^2, RMSD, NRMSD, MBE, and T (1950–2020). Values in the parentheses denote data coverage for GHCN-M.

highly underestimate T_{2m} in comparison with the in situ measurements. For these five stations, mean temperatures of 20.5°C and 22.3°C are obtained for ERA5 and GHCN-M, respectively. This means that the ERA5 T_{2m} are associated with large biases near the Spanish coast.

3.2. Trends in MERRA-2 AOT

In the comparison between MERRA-2 and AERONET, monthly AOT values have been excluded if the number of daily values in a month is less than five. The legend in Figures 3 and 4 shows the mean number of days (nrDays), with corresponding one standard deviation, included in the monthly averaging (April–September). The relatively high nrDays values indicate that there are not many months that have been excluded in the comparison. The figures show relatively good agreement between MERRA-2 and AERONET over the last two decades, on the whole with small deviations in mean AOT and low NRMSD values (15%–30%), with the exception for Birkness (40%) and Gustav Dalen (37%). Based on linear regression for the latest two decades, Table 1 shows that negative trends in AOT are found for all the AERONET and MERRA-2 comparable cases, with the exception for the latter data set (first trend value) and the Birkness, Evora, Gustav Dalen, and Kuopio sites. To capture the trends requires good accuracy in the estimates of AOT, since weak changes appear for these AERONET sites. Even so, large deviation in the trend occurs between AERONET and MERRA-2 also for Brussel. The coarse resolution of the grid boxes for MERRA-2 in combination with poor air quality may be a reason for the deviation that appears for this station. All days are not included in the monthly averaging of AERONET AOT and this may also induce uncertainties in the estimates. The second trend value for MERRA-2 in Table 1 is obtained for the years 1999–2020 corresponding to the AERONET period when all current sites are taken in consideration. Exclusively negative values in MERRA-2 AOT are obtained here. Negative trends in AERONET and MERRA-2 AOT are in line with MODIS observations for approximately the latest two decades (April–September) in Northern Europe (Glantz et al., 2019). The latter study also shows that AOT decreases further north in this region. Figures 3 and 4 show that the highest monthly mean AOT, for both MERRA-2 and AERONET, is found in Central and Eastern Europe, Belsk and Moldova, while the lowest values are found in Northern Europe and in Evora, Southern Europe. Lower AOT values, compared to Central and Easter Europe, are also found at the site Chilbolton, United Kingdom. Furthermore, Figures 3 and 4 show that the strongest reduction in MERRA-2 AOT occurred in the 1980s and 1990s in line with previous studies showing trends in emissions of aerosol precursors and primary aerosols (Sections 1 and 3.5). MERRA-2 AOT has decreased over the stations located in Southern Europe with 21% when comparing decadal means of the 1980s and 2010s, while by 37%–51% for the remaining stations.

3.3. Trends in ERA5 SSRDc for Clear-Sky Condition

Figure 5 shows changes in ERA5 SSRDc during the period 1950–2020 for the same eight ground-based stations as in Figure 1. SSRDc are associated with a minimum around 1975 and an increase with approximately 15 W m^{-2} after 1980. The figures also show a weaker positive trend in SSRDc after around 2000. Results from SBDART simulations, where SSRDc have been averaged for April–September and for each of the latest four decades, show as well significant positive trends (Figure 5). However, the increase in SSRDc from the model simulations is on the whole stronger compared to ERA5. Even so, weaker increase in SSRDc appears on the whole southward in Europe for both ERA5 and SBDART, where the weakest increase is found for the most southerly station Cordoba in Spain. The values of R^2, shown in Figure 5, are obtained for ERA5 SSRDc and MERRA-2 AOT for each site, where the former results are dependent on trends in aerosols from CMIP5.

10.1029/2021JD035889

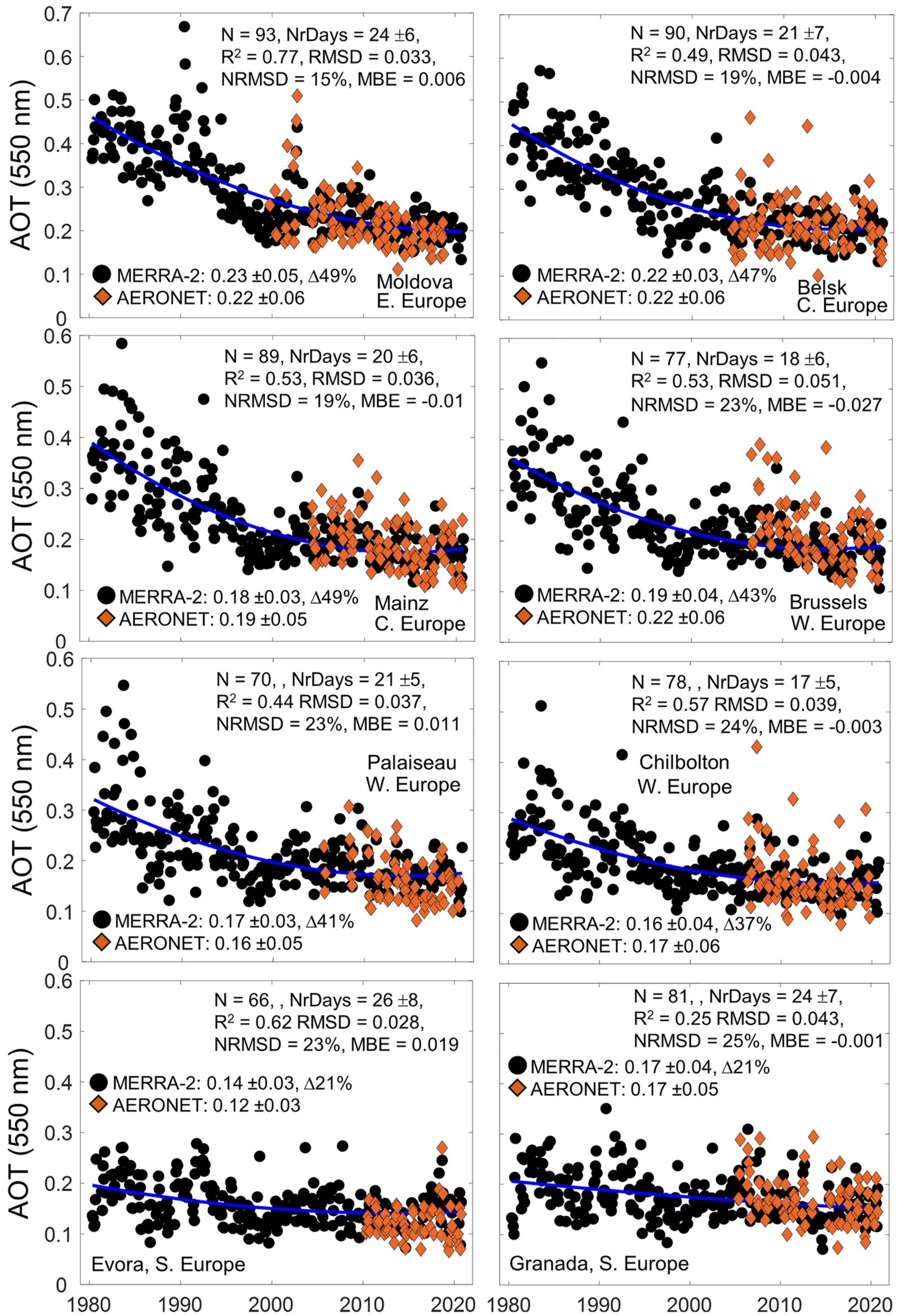

Figure 3. Modern-Era Retrospective analysis for Research and Applications, Version 2 (MERRA-2) monthly aerosol optical thickness (AOT; April–September) for the period 1980–2020 and for eight AErosol RObotic NETwork (AERONET) stations in Europe (Table 1). Decreases in MERRA-2 AOT (in %) is obtained by comparing decadal means for 1980s and 2010s. The blue solid line is a second-order polynomial fit obtained from MERRA-2 monthly AOT values. MERRA-2 monthly AOT is compared to AERONET monthly AOT according to the latter data record (mean values with corresponding one standard deviation are presented), where N is number of months, NrDays is mean number of days with corresponding one standard deviation included in the AERONET monthly averaging, R^2 is coefficient of determination, RMSD is root mean squared deviation, NRMSD is normalized RMSD, and MBE is mean bias error. C., E., S., and W. denote Central, Eastern, Southern, and Western, respectively.

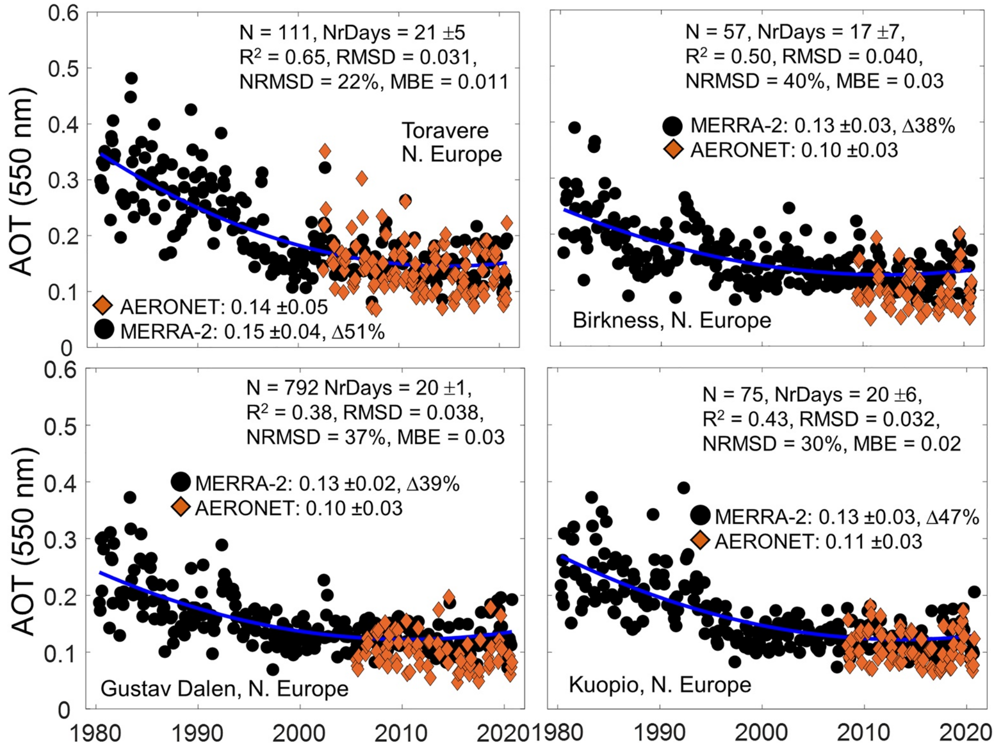

Figure 4. N. denotes Northern. See more information corresponding to Figure 3 about the comparison here for additional four ground-based sites.

3.4. Trends in ERA5 SSRD for All-Sky Conditions

Figures 6 and 7 show validation of ERA5 SSRD against GEBA ground-based measurements for all-sky condition and averaged with respect to April–September. For each of the regions/countries, Eastern Europe, Germany, France, and Iberian Peninsula, in this order, results corresponding to four sites are presented in the figures. Although both ERA5 and GEBA SSRD are associated with large variability, the figures on the whole show also for this quantity, as for SSRDc, a minimum around 1975. Figure 7 suggests however a weaker increase in ERA5 SSRD (orange solid line) after around 1980 for the Iberian Peninsula compared to the other stations. Table 3 shows corresponding comparison of mean SSRD values between ERA5 and GEBA, averaged for stations belonging to the four regions/countries. The table also shows results of positive trend obtained from ERA5 and GEBA SSRD for the period 1979–2020 and 1979–2019, respectively. Some of the GEBA stations are missing data for some of the years within the current period. Data coverage for GEBA with respect to the period 1979–2020 is shown in the parentheses in Table 3. The first trend value for ERA5 (column 10 in Table 3) was calculated for the same years as GEBA. The second trend value for ERA5 is estimated for all years within the period 1979–2020. The statistics in the table show, on the whole, good agreement between the reanalysis and in situ measurements, for example, NRMSD in the range 3.8%–8.4%. The increases in SSRD since 1979 are statistically significant at the 95% confidence level (*F* test) for all the ERA5 cases and GEBA ground-based stations with the exception for Porto and Limoges for the latter data set (not shown). Table 3 shows also that large deviation in the trend is found between ERA5 and GEBA for Iberian Peninsula, which is further discussed in Section 4.

3.5. Trends in Aerosol Precursor, AOT, LCC, SSRDc, and SSRD for Europe

Figure 8a shows changes in worldwide anthropogenic emissions of sulfur dioxide (SO_2, from Smith et al., 2011). A maximum in the emissions is found around 1975 for Europe. Significant negative trends in MERRA-2 AOT are found for Spain and Ukraine since 1980 (Figure 8b). In addition, negative and positive trends in ERA5 SSRDc and SSRD (Figures 8c and 8e, respectively), with a shift that occurred around 1975, are found as well. Figure 8d shows opposite evolution for ERA5 LCC compared to SSRD. The changes for the MERRA-2 and ERA5 quantities are smaller for Spain compared to Ukraine.

10.1029/2021JD035889

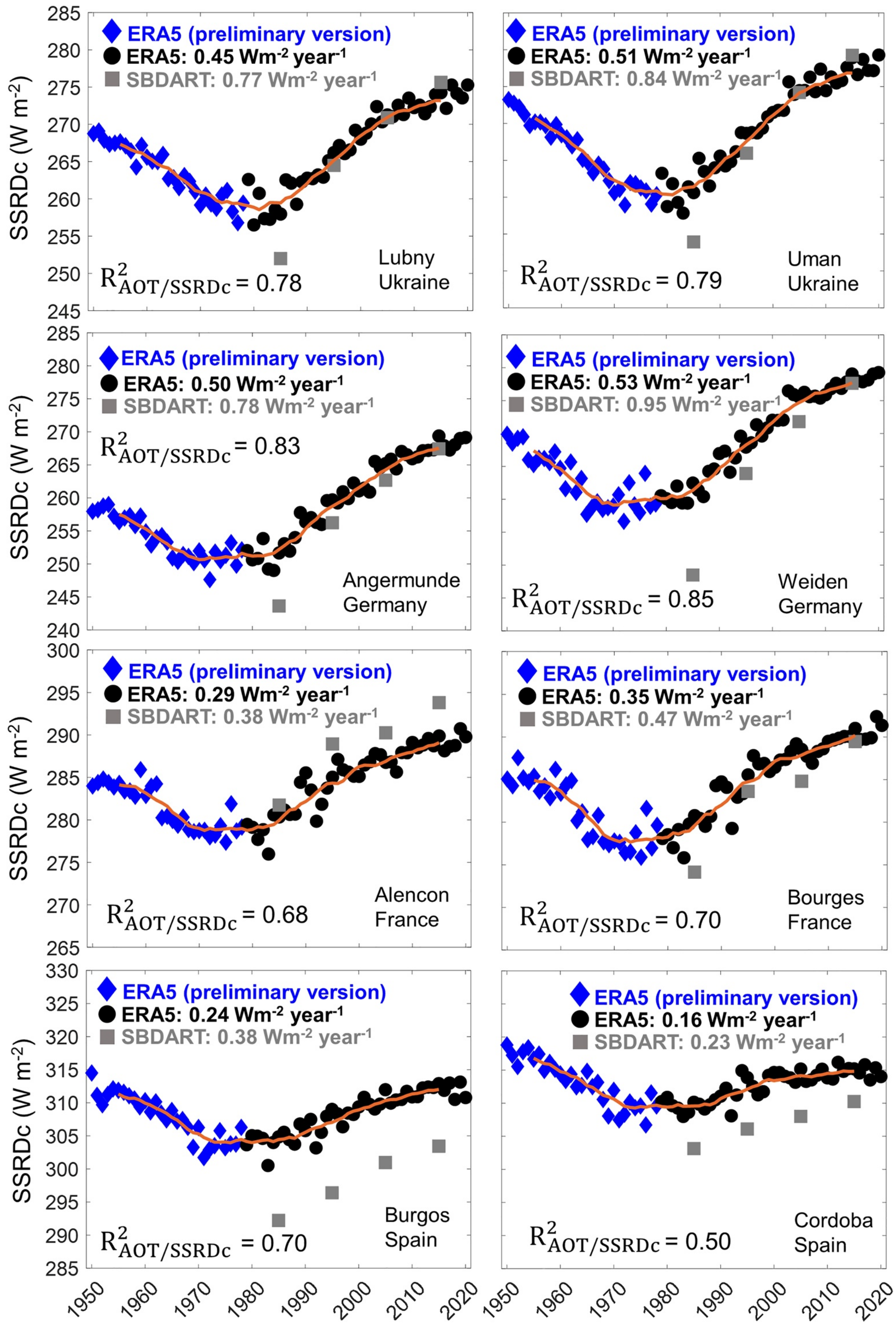

Figure 5. ERA5 surface solar radiation for clear-sky conditions (SSRDc) averaged for the period April–September and the same eight ground-based stations in Figure 1. Solid orange lines denote 10-year running means in regards to the ERA5 mean SSRDc values. Gray squares denote Santa Barbara DISORT Atmospheric Radiative Transfer (SBDART) SSRDc averaged for the period April–September and for each of the decades 1980s, 1990s, 2000s, and 2010s. Values of coefficient of determination (R^2) are obtained from linear regression between Modern-Era Retrospective analysis for Research and Applications, Version 2 (MERRA-2) aerosol optical thickness (AOT) and ERA5 SSRDc.

10.1029/2021JD035889

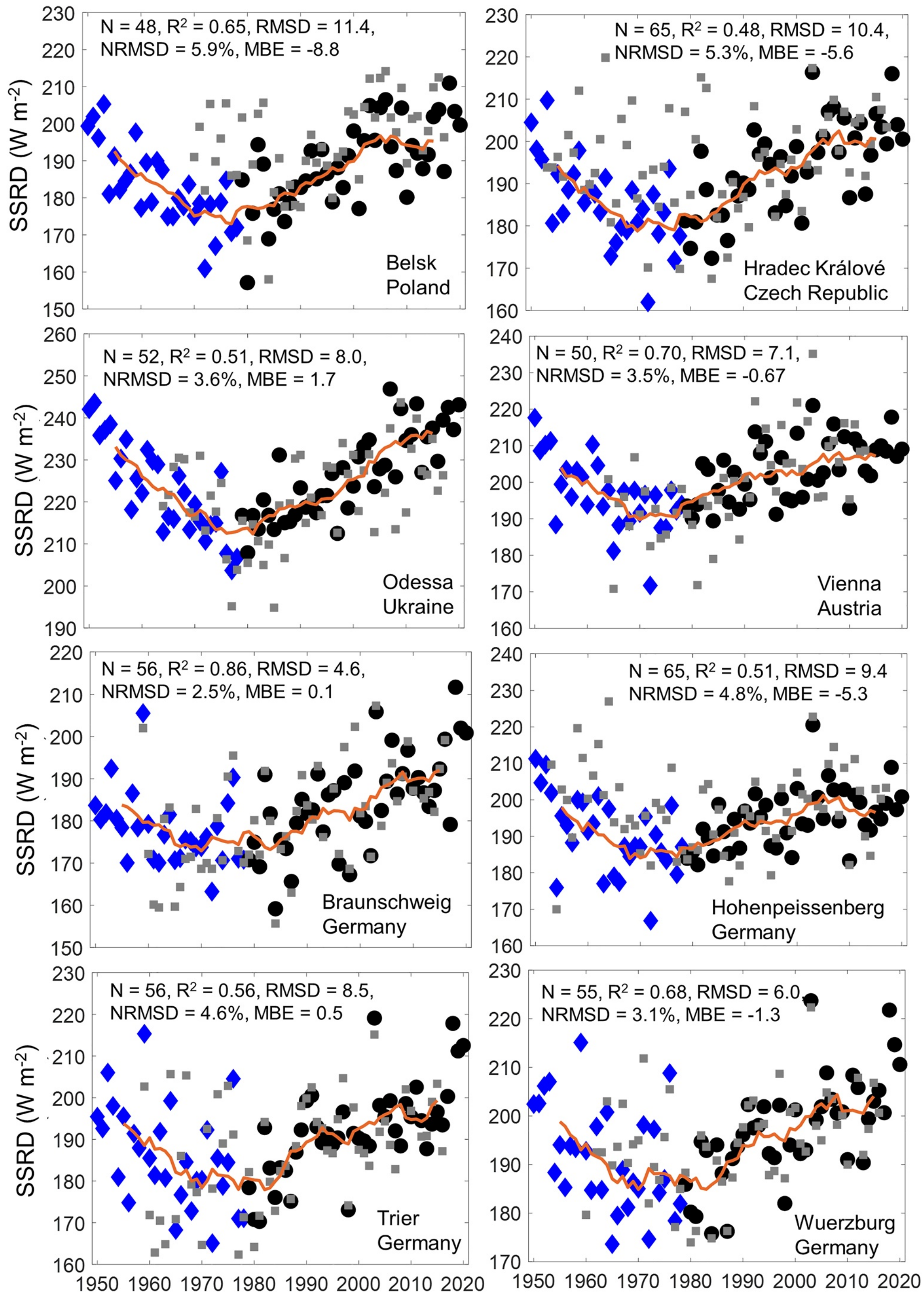

Figure 6. Comparison between downward surface solar radiation for all-sky conditions (SSRD) from ERA5 reanalysis and Global Energy Balance Archive (GEBA) ground-based measurements in the period April–September. The blue diamonds and black circles represent ERA5 SSRD according to the periods 1950–1978 (preliminary version) and 1979–2020 (final release), respectively. The gray squares denote GEBA SSRD for years where data are available. Solid orange line denotes 10-year running means of ERA5 mean SSRD values. See information corresponding to Figure 1 about the statistical analyses used. Information about the sites are given in Table A2.

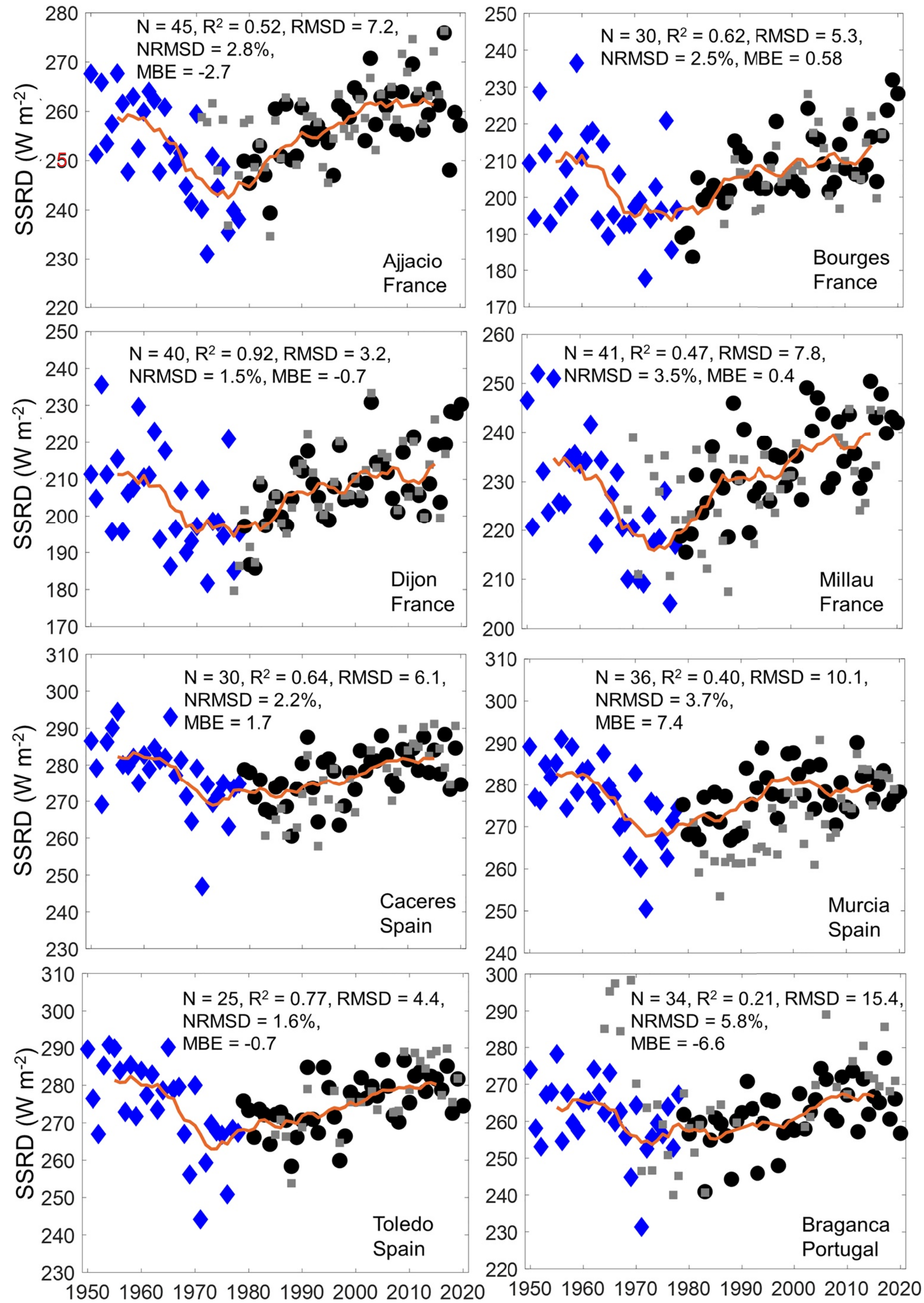

Figure 7. See information corresponding to Figure 6 about the comparison here for additional eight ground-based sites.

3.6. Warming in Europe Due To Decline in Aerosols and Enhanced Greenhouse Effect

3.6.1. Unmasked Direct Aerosol Effect

Figures 9a and 9b show MERRA-2 AOTs over Europe, averaged for April–September and over the 1980s and 2010s, respectively. The figures show indirectly that the highest concentrations of aerosols in the 1980s were present over Central and Eastern Europe. This finding is consistent with results of ERA5 SSRDc, where strong positive changes up to about 20 W m^{-2} between the decadal means of the 1980s and 2010s are found for this region (Figure 9c). By

Table 3
Comparison Between ERA5 and GEBA Mean SSRD and Trend (ΔSSRD) for the Periods 1950–2019 and 1979–2020, Respectively (April–September)

Country/region	N_{sites}[a]/N_{all}[b]	R^2	RMSD ($W\ m^{-2}$)	NRMSD (%)	MBE ($W\ m^{-2}$)	$SSRD^{GEBA}$ ($W\ m^{-2}$)	$SSRD^{ERA5}$ ($W\ m^{-2}$)	$\Delta SSRD^{GEBA}$ ($W\ m^{-2}\ year^{-1}$)	$\Delta SSRD^{ERA5}$ ($W\ m^{-2}\ year^{-1}$)
Eastern Europe	8/423 (90%)	0.58	13.0	6.7	−0.4	194 ± 20	193 ± 16	0.54 ± 0.15	0.48 ± 0.17
									0.50 ± 0.16
Germany	6/338 (82%)	0.71	7.3	3.8	−2.1	191 ± 13	188 ± 12	0.52 ± 0.16	0.44 ± 0.09
									0.52 ± 0.12
France	8/315 (78%)	0.88	8.9	4.0	−2.0	221 ± 25	219 ± 23	0.45 ± 0.14	0.46 ± 0.08
									0.49 ± 0.10
Iberian Peninsula	7/232 (64%)	0.38	12.5	4.6	1.2	272 ± 15	273 ± 13	0.54 ± 0.11	0.30 ± 0.09
									0.25 ± 0.05

Note. RMSD, NRMSD, and MBE (1950–2019). Percentage values in the parentheses (column 2) denote data coverage for $\Delta SSRD^{GEBA}$ with respect to the period 1979–2020. The first and second trend values for ERA5 (column 10) are obtained for the same years as GEBA and the period 1970–2020, respectively.
[a]Number of GEBA sites. [b]Number of compared values in the calculations of R^2.

applying the present approach on ΔSSRDc (Section 2.3) and comparing decadal means of the 1980s and 2010s, significant increases in T_{SSRDc} are estimated, with about 1°C warming for Central and Eastern Europe (Figure 9d). The increases in T_{SSRDc}, likely caused by decreases in aerosols, can be compared to total warming (ΔT_{STRUc}) for clear-sky conditions (Figure 9e). In addition, mean values of ΔT_{SSRDc} presented in Table 4 can be compared to total warming for clear-sky conditions in Figure 2 (right panel), for the four countries. From this, we see that the ΔT_{SSRDc} is substantially weaker for Germany, France, and Spain, while ΔT_{STRUc} is strong for both Ukraine and Spain. Furthermore, Figure 9f shows changes in net radiation for clear-sky conditions (ΔNetRadc), which reflect differences between downward and upward ERA5 surface solar radiation plus surface terrestrial radiation between 2010s and 1980s. For the Alps and Carpathian Mountains, decreases in snow cover likely explain increases in NetRadc. The increases in NetRadc, shown in the figure for the Arctic region, northern Baltic Sea, and Gulf of Finland, are caused by decreases in sea ice (not shown) during the latest four decades. This in turn explains increases in T_{STRUc} in these areas. Note, the strong warming found for the Iberian Peninsula appears simultaneously as a weaker decrease and increase in AOT and SSRDc, respectively, have occurred in this region. While Central and Eastern Europe have experienced a significant increase in NetRadc, the latter quantity is largely unchanged for the Iberian Peninsula.

3.6.2. Warming in Europe for All-Sky Conditions

Figures 10a and 10b show substantially reduced April–September mean ERA5 LCC and TCC, respectively, for large parts of Europe during the latest four decades. Figures 10c and 10d show increases in SSRD and T_{SSRD}, respectively, over the same period for all-sky conditions. By comparing decadal means of the 1980s and 2010s, significant increases in T_{SSRD} are estimated, with even larger warming for some parts of Europe compared to clear-sky conditions (Figure 9d). The total warming (ΔT_{2m}) observed in Europe for all-sky conditions is shown in Figure 10e. Mean values of ΔT_{SSRD} presented in Table 4 for all-sky conditions can be compared to ΔT_{2m} in Figure 2, for the four countries. As for the clear-sky situation, the ΔT_{SSRD} is substantially weaker southward. Simultaneously, the ΔT_{2m} is somewhat weaker here for Spain compared to clear-sky conditions. The increases in NetRad over Central and Eastern Europe are somewhat lower for all-sky conditions, shown in Figure 10f, compared to the clear-sky situation (Figure 9f). Small changes in NetRad, as well as in NetRadc (Figure 9f), on the whole occur for Iberian Peninsula (Figure 10f). The latter is in line with weaker increase in SSRD (Figures 8e and 10c) for this region, as well as in SSRDc for clear-sky conditions, coincident with an increase in sensible heat flux (Section 3.6.3). The latter means enhanced surface warming due to less evaporative cooling (Section 4), which in turn is expected to increase STRU and STRUc. A land-sea mask has been included in Figure 10d to screen out ocean areas. This is because energy from absorbed solar radiation is distributed in the ocean column, dependent on the depth. The role of the ocean is thus not accounted for in the present approach, based on radiation balance at the surface, to estimate warming caused by changes in SSRD.

3.6.3. Changes in Surface Albedo, Sensible, and Latent Heat Fluxes

Figures 11a and 11b show changes in the present factors (Δ(SSRU/SSRD) and Δ(HF/SNSR) in Equation 1) used to adjust for the surface albedo effect and the energy that is converted to HF, respectively, for all-sky conditions

10.1029/2021JD035889

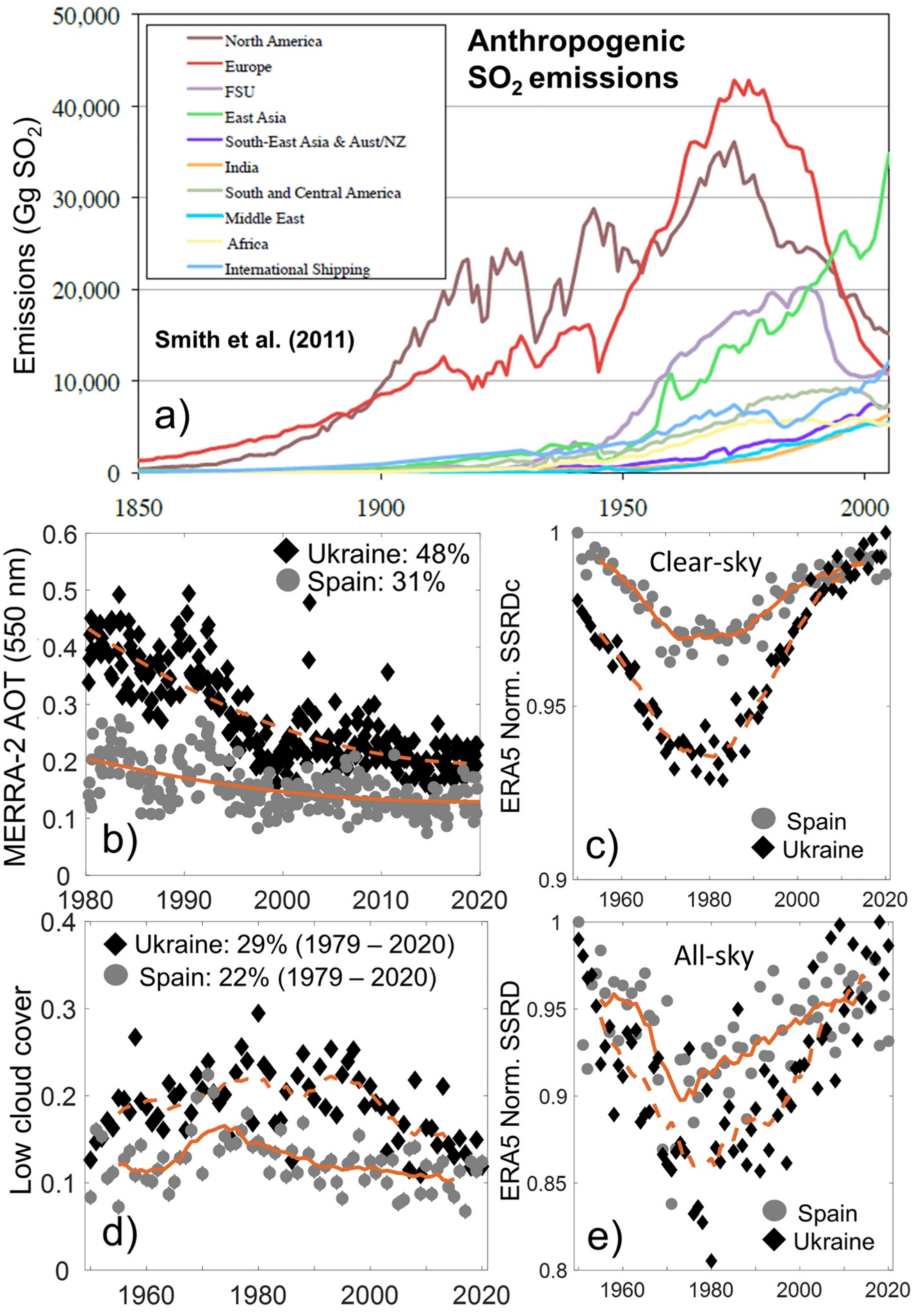

Figure 8. (a) Global anthropogenic SO_2 emissions from Smith et al. (2011). (b) Modern-Era Retrospective analysis for Research and Applications, Version 2 (MERRA-2) mean aerosol optical thickness (AOT), (c) ERA5 mean surface solar radiation downward for clear-sky conditions (SSRDc), (d) ERA5 mean low cloud cover (LCC), and (e) ERA5 mean surface solar radiation downward for all-sky conditions averaged for April–September with respect to Spain (37°N–42°N, 5°W–1°W) and Ukraine (46°N–50°N, 27°E–34°E). Decreases in AOT and LCC (in percent) are obtained by comparing the 1980s and 2010s. Orange solid and dashed lines in (b) and (c)–(e) denote second-order polynomial fit and 10-year running means, respectively.

and by comparing decadal means of 1980s and 2010s. Although Figure 11b shows positive trends in HF/SNSR for large parts of Central and Eastern Europe and negative trends over France and Spain, the changes are relatively small (below 5%). The factor describing changes in the SSRU/SSRD has generally somewhat decreased (less than 5%), although larger decreases are found for example, for the Nordic countries and the Alps (Figure 11a) where snow cover has decreased. By including HF as a residual and considering also changes in the surface albedo,

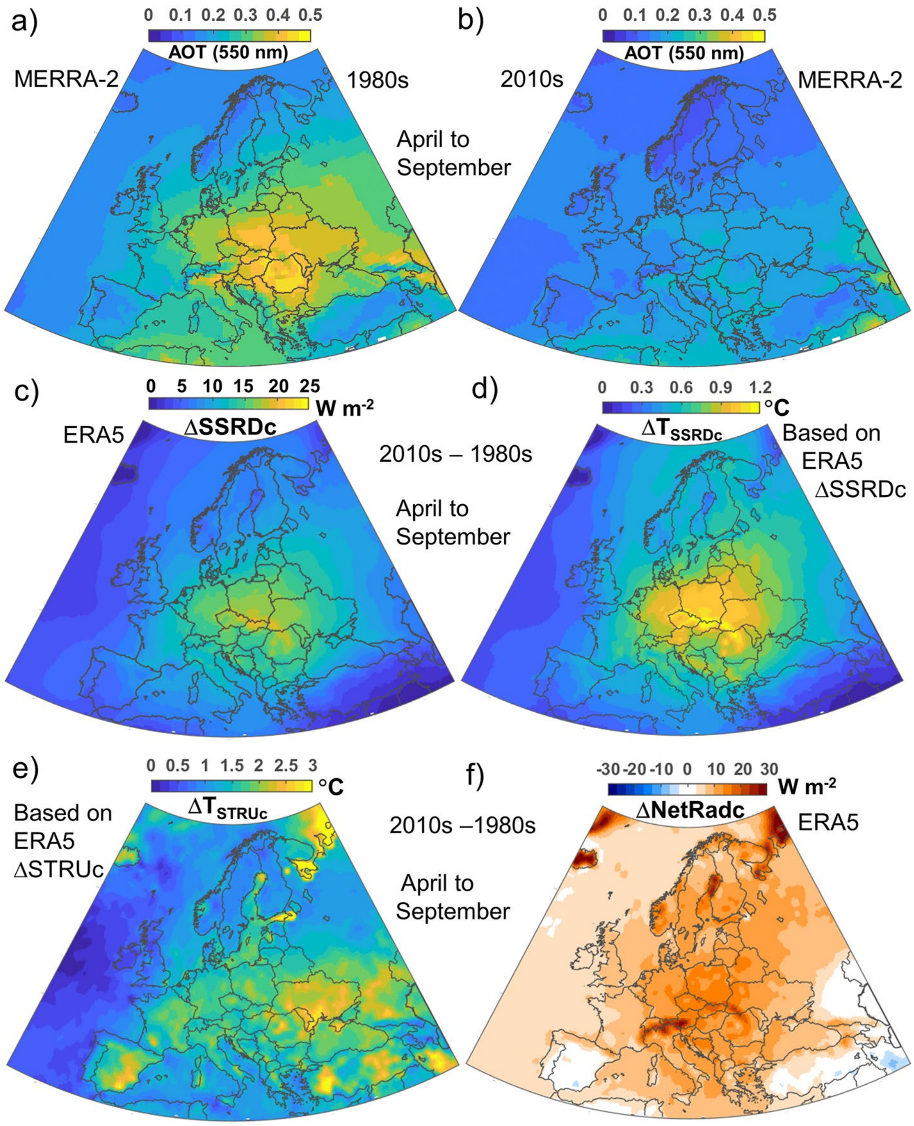

Figure 9. Modern-Era Retrospective analysis for Research and Applications, Version 2 (MERRA2) decadal mean aerosol optical thickness (AOT) for April–September during (a) 1980s and (b) 2010s. Changes in (c) downward surface solar radiation (SSRDc), (d) near surface temperature (T_{SSRDc}) estimated based on changes in SSRDc, (e) near surface temperature (T_{STRUc}) estimated based on changes in upward surface terrestrial radiation upward (STRUc), and (f) net radiation (NetRadc: surface solar radiation plus terrestrial radiation downward minus upward) with respect to clear-sky conditions, April–September, and by comparing 1980s and 2010s.

Table 4
Increase in Temperature, Estimated Based on the Present Method for Clear-Sky and All-Sky Conditions (ΔT_{SSRDc} and ΔT_{SSRD}, Respectively), by Comparing Decadal Means of the 1980s and 2010s (April–September)

Country	N[a]	ΔT_{SSRDc}	ΔT_{SSRD}
Ukraine	5	0.83 ± 0.12	1.13 ± 0.20
Germany	16	0.89 ± 0.07	0.85 ± 0.19
France	9	0.49 ± 0.08	0.71 ± 0.22
Spain	13	0.38 ± 0.07	0.34 ± 0.11

[a]Number of sites included in the estimates (Table A1).

similar results are obtained for the two rates for clear-sky conditions as for the all-sky situation (not shown). Furthermore, Figures 11c and 11d show changes in SSHF and SLHF, respectively, by comparing the two decades. Positive trends in these two quantities are shown in the figure for nearly all Europe, with the exception for SLHF and particularly Spain. The latter means that very small increases in HF are found for Iberian Peninsula (not shown), in line with the results of NetRad (Figure 10f). Furthermore, Figures 11e and 11f show changes in the factors SSHF/SNSR and SLHF/SNSR, respectively, by comparing the decadal means of 1980s and 2010s. Although small changes are found in the factor associated with HF (Figure 11b), the figures show that the relative contribution between SSHF and SLHF may differ regionally. Most of Europe experiences an increase in SSHF/SNSR with a

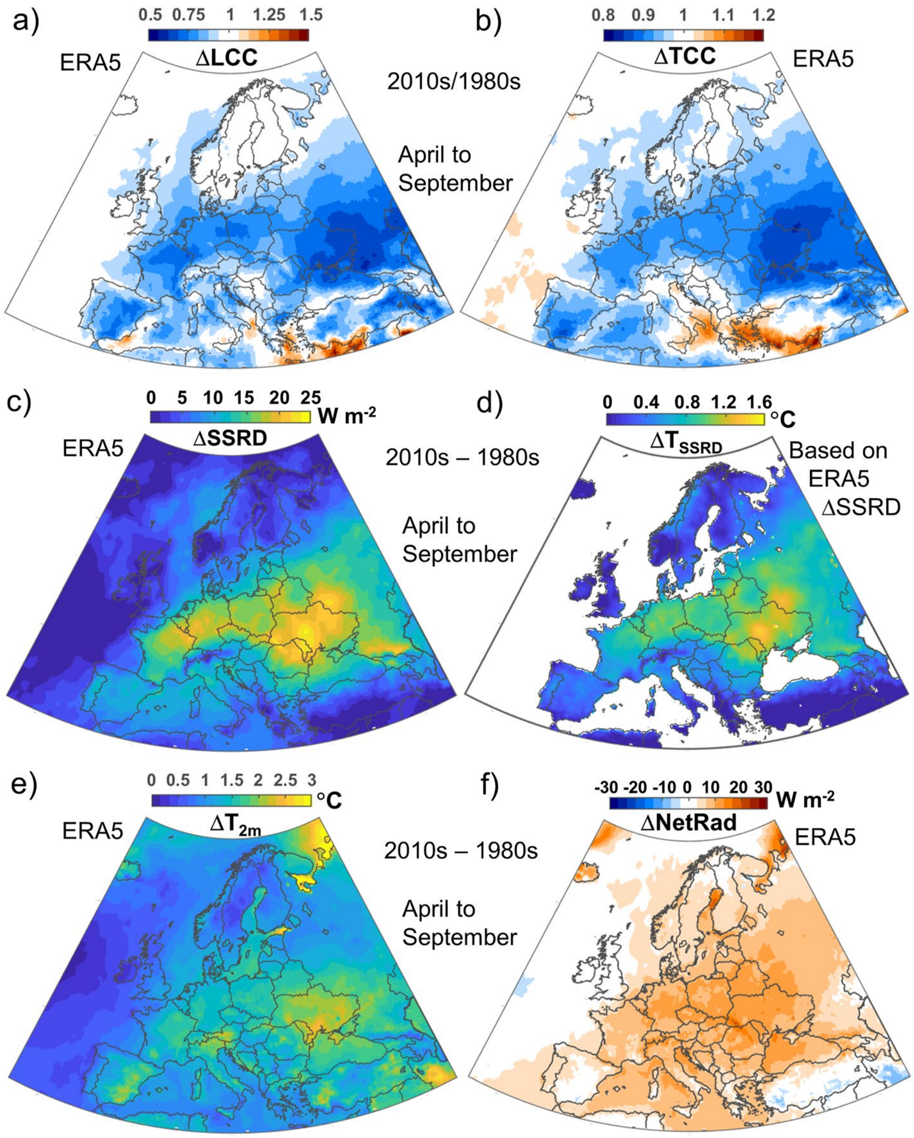

Figure 10. Changes in (a) low cloud cover (LCC), (b) total cloud cover (TCC), (c) surface solar radiation downward (SSRD), (d) near surface temperature (T_{SSRD}) estimated based on changes in SSRD, (e) temperature derived at 2 m (T_{2m}), and (f) net radiation (NetRadc: surface solar radiation plus terrestrial radiation downward minus upward) for all-sky conditions during April–September, and comparing 1980s and 2010s.

concurrent decrease in SLHF/SNSR. The largest changes are found for the Iberian Peninsula in line with strongest decreases in evaporation of equivalent water found for this region during the latest four decades (not shown). These findings are further discussed in the following section.

4. Discussion

Heat flux is not available in the ERA5 data sets for clear-sky condition but has been estimated as the residual considering a radiation balance between net solar radiation and net terrestrial radiation. Heat flux is available for ERA5 all-sky conditions. However, a complete radiation balance cannot be established for all-sky conditions. For example, net energy of 5 W m^{-2} toward the surface over Central Europe is found for both 1980s and 2010. This is probably caused by the assimilation system that is not conserving energy. Nevertheless, this amount of 5 W m^{-2} constitutes less than 3% of the SSRD for both decades. In addition, by comparing SSRDc and SSRD for Central Europe after 1950, a substantially larger variability is found for SSRD. SSRDc is instead associated with a smoother change over

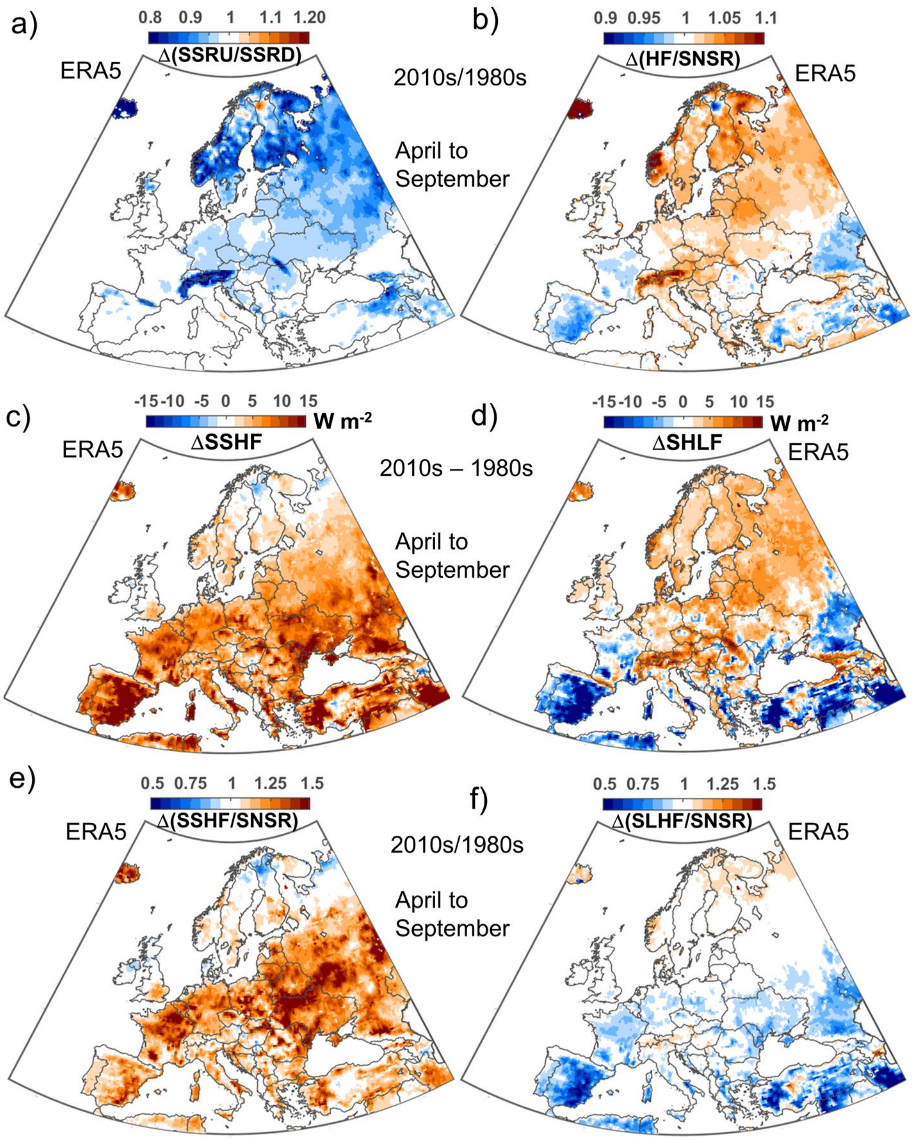

Figure 11. Changes in (a) surface solar radiation upward (SSRU) divided by surface solar radiation downward (SSRD), (b) heat flux (HF) divided by surface net solar radiation (SNSR), (c) surface sensible heat flux (SSHF), (d) surface latent heat flux (SLHF), (e) SSHF divided by SNSR, and (f) SLHF divided by SNSR with respect to all-sky conditions, April–September, and by comparing 1980s and 2010s.

the seven decades, as expected due to the absence of cloud effects. By including heat flux as a residual, we therefore assume minor errors induced in the estimates of near surface temperature for clear-sky conditions over land.

Considering also the preliminary results of ERA5 SSRDc and SSRD (1950–1978), Figures 8c and 8e, respectively, show clearly two periods associated with "dimming" and "brightening," where a change in the sign of the trend occurred around 1975. The increases in SSRD and SSRDc, by comparing decadal means for 1980s and 2010s, have been used in the present approach to estimate changes in near surface temperature. For clear-sky and all-sky conditions, the temperature increase is as much as about 1°C for Central and Eastern Europe. The total warming over the period 1980–2020 for clear-sky conditions, reflected by T_{STRUc}, is about 2°C in these regions as well as in Spain. Lower total warming is on the whole found for all-sky conditions (Figure 2). Furthermore, the present approach dealing with monthly averaging in the estimates of warming does not take in consideration a reduced greenhouse effect due to decrease in cloud cover. The latter effect cannot be separated, and estimated, from the counteracted effect caused by increases in the GHGs during the four decades. This means that the warming estimated here for all-sky conditions is probably overestimated, maybe with exception and wrong reason for the Iberian Peninsula (see below). Even so, a reduced indirect aerosol effect after 1980, reflected by a decrease in cloud cover and an increase in SSRD, may have contributed to a rapid warming over large parts of Europe. However, decreased cloud cover could also be a result of cloud and soil moisture feedbacks from the initial temperature perturbation caused by the enhanced greenhouse effect. Natural internal variability may also play a role for these changes.

Considering the present investigation areas (Table 3), the factors used in the present approach to adjust for the albedo effect and energy that is converted to HF are associated with relatively small changes (less than 5%) over the four decades (Figures 11a and 11b). However, this study also shows that relatively more of solar energy was converted to SSHF at the expense of SLHF in the 2010s than in the 1980s. If this shift between latent and sensible heat fluxes is a result of the decrease in aerosols, the impact goes well beyond increasing the temperature locally and is probably influencing additional processes as well. For example, a reduction in latent heat flux may result in less cloudiness, and an increase in sensible heat flux near the surface may increase the temperature elsewhere in the atmosphere through convection and advection. Nevertheless, this change in the distribution of heat flux has no impact on the present approach to estimate warming due to decline in aerosols, since the estimates represent mean conditions for the summer half year. However, more of sensible energy at the expense of latent energy is indicative of larger daily variation in the temperature, thus, a higher daily maximum temperature.

The comparison of the trends between ERA5 and GEBA for the Iberian Peninsula suggests an underestimation in SSRD changes for the former data set. This in turn may influences the warming estimated based on the present approach. At the same time, Table 3 shows relatively low data coverage for GEBA over the Iberian Peninsula that may reduce the representativeness of the corresponding results. However, by using more stations than the ones included in the GEBA data set. although for a somewhat shorter investigation period, 1985–2010, Sanchez-Lorenzo et al. (2013) found similar magnitude of the brightening trends over this region to those presented here. One reason for the deviation in the trends between ERA5 and GEBA SSRD may be that the former overestimate decreases in cloudiness over the Iberian Peninsula. Furthermore, the present results of SSRDc are associated with substantially smaller variability compared to SSRD due to the absence of clouds. The trends in SSRDc are, as well as for SSRD, weaker for Iberian Peninsula. Nevertheless, a validation of SSRDc is required and important to perform when ground-based measurements are available for Europe. Furthermore, the largest changes in the contributions to HF from SSHF and SLHF during the latest four decades are found for Iberian Peninsula. At the same time, the present results suggest a weaker effect from the aerosols on the solar radiation, but a large change in near surface temperature. The total warming for Spain (Figure 2) is, for both all-sky and clear-sky conditions, substantially larger than the changes in T_{SSRDc} and $\mathrm{T}_{\mathrm{SRRD}}$ (Table 2). Causes for changes in the distribution of HF can be several, but a change in the surface properties is an obvious reason and possible feedback mechanism from increases in SNSR and GHGs. Changes in lateral transport of HF to the region may also play a role. Drier summers due to soil moisture–precipitation feedbacks in Southern Europe is another explanation (Tuel & Eltahir, 2021). Drying and depletion of soil moisture leads to enhanced surface warming due to less evaporative cooling, which in turn increase sensible heat that warms the lowest air layers. A decrease in evaporation likely causes a reduction in cloudiness. Mateos et al. (2014) found that a positive trend in SSRD between 2003 and 2012 was mainly caused by reductions in clouds (75%) and the remaining part due to decline in aerosols (25%). The shift of the subtropical climate zone toward higher latitudes, a finding from previous studies (Section 1), may also result in a temperature increase without a corresponding change in SSRD. The present findings are in line with results reported by Christidis and Stott (2021) that indicate summertime widespread dryer conditions for the last decades, which are more extreme in Southern Europe. They demonstrate that anthropogenic forcing drives marked changes in European summers. Thus, the rapid total warming over the Iberian Peninsula is probably caused by greenhouse warming, more arid surfaces, and to some degree decline in aerosols. Tropical expansion may have contributed to drier surface conditions and reduced cloud cover in this region.

The largest decreases in sulfur dioxide (Smith et al., 2011) and MERRA-2 AOT over Europe have occurred in the 1980s and 1990s. Atmospheric aerosols have continued to decrease after 2000, although at a substantially slower rate. This is in line with a weaker increase in SSRDc after around 2000 for Ukraine and Spain (Figure 8c) found in ERA5. This suggests similar changes in the aerosols prescribed in ERA5 over the four decades. The monthly averaged aerosol concentrations in Europe are still somewhat elevated today due to man-made activities compared to background conditions. Despite the change in the rate of decrease of AOT, the total warming in Central and Eastern Europe has however increased at more or less the same rate after 1980, although somewhat faster for clear-sky condition compared to the all-sky situation. Beside enhanced greenhouse effect and reduced impacts from the aerosols, previous studies suggest changes in atmospheric circulation (Blanc et al., 2022; Sfică et al., 2020), which may have contributed to the rapid warming. The present finding of a substantial warming in Europe due to decreases in aerosols in addition to greenhouse warming is important and relevant when considering other regions on Earth in the future. The concentrations of aerosols are in many regions in Asia at the same level or even higher today compared to what the most polluted countries in Europe experienced in the 1980s. Even so, anthropogenic aerosols have started to decline in China during the latest decade (Tao et al., 2020).

Trends in warming for marine areas corresponding to the arctic region north of Scandinavia, as well as for Bothnia Bay, Bothnia Sea, and Gulf of Finland, are explained mainly by reduction in sea ice, higher absorption of solar radiation, and increases in heat flux (not shown). This positive feedback is likely to be active primarily in April and May, particularly for the more southerly located Bothnia Sea and Gulf of Finland. Even so, the present results show that the surface albedo effect has still a significant influence on the near surface temperature also when averaging with respect to April–September.

5. Conclusions

Increases in solar radiation reaching the surface caused by decreases in aerosols during the period 1979–2020 and between the months April and September have led to an enhanced increase in near surface temperature of as much as about 1°C for clear-sky conditions and somewhat more for all-sky conditions in Central and Eastern Europe. This means that also other regions on Earth with current high anthropogenic aerosol loadings will probably experience warming if aerosol concentrations are to decrease in the future. The total warming observed during clear-sky conditions of the latest four decades is for large parts of Europe double the change in global annual mean temperature of about 1.1°C, while somewhat lower for all-sky conditions. Although the largest effects from aerosols on the radiation balance occurred in the 1980s and 1990s, the total warming has continued to increase more or less at the same rates during the latest four decades over large parts of Europe, considering both all-sky and clear-sky situations. Thus, decline in aerosols can certainly not explain all warming observed and particularly not considering the southern Iberian Peninsula. The largest increases in sensible heat flux at the expense of latent heat flux have occurred in this region, which is probably a result of drier surface conditions. This means a positive feedback associated with reduced evaporate cooling, while decline in water vapor may also have contributed to decreased cloud cover. Increased sensible heat flux in turn means warming of the lowest air layers. Anthropogenic aerosols over large parts of Europe have thus temporarily masked, until around 1980, parts of rapid warming from increases in GHGs. CO_2 from fossil fuels is of particularly serious concern, since it can continue to affect climate for thousand years. The large regional effect found in this study suggests also the importance for improvements of descriptions of climate drivers in regional and global climate models to realistically assess future climate change.

Appendix A: Basic Information About Ground-Based Stations

Tables A1 and A2 show basic information about ground-based stations, where temperature and SSRD, respectively, have been investigated in the present study.

Table A1
Global Historical Climatology Network-Monthly (GHCN-M) Version 4 Data Set of Monthly Mean Temperature

Site	Country	Condition	Latitude	Longitude	Altitude (m)	Period	Status[a]
Lubny	Ukraine	Inland	50.0°N	33.0°E	156 m	1950–2020	Included
Poltava	Ukraine	Inland	49.6°N	34.6°E	160 m	1950–2020	Included
Uman	Ukraine	Inland	48.8°N	30.2°E	214 m	1950–2020	Included
Shepetivka	Ukraine	Inland	50.2°N	27.1°E	277 m	1950–2020	Included
Askania-Nova	Ukraine	Near coast	46.5°N	33.9°E	28 m	1950–2019	Included
Altomunster	Germany	Inland	48.4°N	11.3°E	510 m	1955–2020	Included
Angermunde	Germany	Near coast	53.0°N	14.0°E	54 m	1950–2020	Included

Table A1
Continued

Site	Country	Condition	Latitude	Longitude	Altitude (m)	Period	Status[a]
Bad Hersfeld	Germany	Inland	50.9°N	9.7°E	272 m	1950–2020	Included
Bad Konigshofen	Germany	Inland	50.3°N	10.4°E	288 m	1951–2020	Included
Berlin Schonefeld	Germany	Inland	52.4°N	13.5°E	46 m	1957–2020	Included
Diepholz	Germany	Near coast	52.6°N	8.3°E	39 m	1953–2020	Included
Hamburg	Germany	Near coast	53.6°N	9.99°E	11 m	1950–2020	Included
Kempten	Germany	Inland	47.7°N	10.3°E	750 m	1950–2020	Included
Koln/Bonn	Germany	Inland	50.9°N	7.2°E	92 m	1950–2002	Included
Lingen	Germany	Inland	52.5°N	7.3°E	22 m	1950–2019	Included
Ruppertsecken	Germany	Inland	49.6°N	7.9°E	461 m	1951–2020	Included
Schleswig	Germany	Near coast	54.5°N	9.5°E	43 m	1950–2020	Included
Simbach Inn	Germany	Inland	48.3°N	13.0°E	360 m	1951–2020	Included
Villingen-Schwenningen	Germany	Inland	48.0°N	8.5°E	720 m	1950–2020	Included
Weiden	Germany	Inland	49.67°N	12.2°E	440 m	1950–2020	Included
Zeitz	Germany	Inland	51.10°N	12.1°E	170 m	1953–2020	Included
Ajaccio	France	Near coast	41.9°N	8.8°E	5 m	1950–2020	Included
Alencon Valframbert	France	Near coast	48.4°N	0.1°E	143 m	1950–2020	Included
Bourges	France	Inland	47.1°N	2.4°E	161 m	1950–2020	Included
Brest	France	Near coast	48.4°N	4.4°W	94 m	1950–2020	Included
Montelimar	France	Inland	44.6°N	4.7°E	73 m	1950–2020	Included
Montpellier	France	Coastal	43.6°N	4.0°E	2 m	1950–2020	Included
Nantes	France	Near coast	47.2°N	1.6°W	26 m	1950–2020	Included
Rennes	France	Near coast	48.1°N	1.7°W	36 m	1950–2020	Included
Toulouse	France	Near coast	43.6°N	1.4°E	151 m	1950–2020	Included
Albacete	Spain	Inland	39.0°N	1.9°W	704 m	1950–2020	Included
Alicante	Spain	Coastal	38.3°N	0.6°W	43 m	1973–2020	Excluded
Bilbao	Spain	Near coast	43.3°N	2.9°W	42 m	1950–2020	Included
Burgos	Spain	Inland	42.4°N	3.6°W	890 m	1950–2020	Included
Cordoba	Spain	Inland	37.8°N	4.8°W	90 m	1956–2020	Included
Coruna	Spain	Coastal	43.4°N	8.4°W	58 m	1950–2020	Excluded
Daroca	Spain	Inland	41.1°N	1.4°W	779 m	1950–2020	Included
Logrono	Spain	Near coast	42.5°N	2.3°W	353 m	1950–2020	Included
Madrid	Spain	Inland	40.4°N	3.8°W	687 m	1950–2020	Included
Malaga	Spain	Coastal	36.7°N	4.5°W	7 m	1950–2020	Excluded
Murcia	Spain	Near coast	38.0°N	1.2 °W	85 m	1950–2020	Included
Ponferrada	Spain	Near coast	42.6°N	6.6°W	534 m	1951–2020	Excluded
Salamanca	Spain	Inland	41.0°N	5.5°W	790 m	1950–2020	Included
Sevilla	Spain	Near coast	37.4°N	5.9°W	34 m	1951–2020	Included
Soria	Spain	Inland	41.8°N	2.5°W	1,082 m	1950–2020	Included
Tortosa	Spain	Coastal	40.8°N	0.5°E	44 m	1950–2020	Excluded
Valencia	Spain	Coastal	39.5°N	0.5°E	69 m	1973–2020	Excluded
Valladoid	Spain	Inland	41.7°N	4.9°W	846 m	1950–2020	Included
Zaragoza	Spain	Inland	41.7°N	1.0°W	247 m	1950–2020	Included

[a]Included or excluded in the present study.

Table A2
GEBA Ground-Based Stations for Measurements of SSRD

Site	Country	Condition	Latitude	Longitude	Elevation (m)	Period
Belsk	Poland	Inland	51.83°N	20.78°E	180 m	1970–2017
Hradec Králové	Czech Rep.	Inland	50.25°N	15.85°E	241 m	1953–2017
Klagenfurt	Austria	Inland	46.65°N	14.33°E	452 m	1964–2017
Odessa	Ukraine	Coastal	46.48°N	30.63°E	64 m	1964–2017
Salzburg	Austria	Inland	47.80°N	13.00°E	435 m	1964–2017
Vienna	Austria	Inland	48.25°N	16.37°E	202 m	1964–2013
Warsawa	Poland	Inland	52.27°N	20.98°E	130 m	1964–2017
Zakopane	Poland	Inland	49.28°N	19.97°E	857 m	1964–2017
Braunschweig	Germany	Inland	52.30°N	10.45°E	81 m	1959–2016
Hohenpeissenberg	Germany	Inland	47.80°N	11.02°E	990 m	1979–2017
Potsdam	Germany	Inland	52.38°N	13.10°E	33 m	1979–2005
Trier	Germany	Inland	49.75°N	6.67°E	278 m	1958–2017
Weihenstephan	Germany	Inland	48.40°N	11.70°E	469 m	1961–2017
Wuerzburg	Germany	Inland	49.77°N	9.97°E	275 m	1957–2017
Ajaccio	France	Coastal	41.92°N	8.80°E	4 m	1970–2017
Bourges	France	Inland	47.07°N	2.37°E	161 m	1987–2017
Dijon	France	Inland	47.27°N	5.08°E	222 m	1976–2017
Limoges	France	Inland	45.82°N	1.28°E	282 m	1967–2013
Millau	France	Near Coastal	44.12°N	3.02°E	715 m	1967–2017
Nancy-Essey	France	Inland	48.68°N	6.22°E	225 m	1967–2010
Nice	France	Coastal	43.69°N	7.27°E	4 m	1967–2017
Reims	France	Inland	49.30°N	4.03°E	95 m	1974–2010
Braganca	Portugal	Inland	41.80°N	6.73°W	691 m	1964–2019
Caceres	Spain	Inland	39.47°N	6.33°W	405 m	1983–2019
Faro	Portugal	Coastal	37.02°N	7.93°W	8 m	1964–2019
Madrid	Spain	Inland	40.45°N	3.72°W	664 m	1964–2019
Murcia	Spain	Near Coastal	37.99 N	1.27°W	61 m	1981–2019
Porto	Portugal	Coastal	41.13°N	8.60°W	93 m	1964–2013
Toledo	Spain	Inland	39.55°N	4.33°W	910 m	1983–2019

Data Availability Statement

How to access ERA5 meteorological data from 1950 to the present is explained on the ECMWF website: https://confluence.ecmwf.int/display/CKB/How+to+download+ERA5#HowtodownloadERA5-OptionB:Download-ERA5familydatathatisNOTlistedintheCDSonlinecatalogue-SLOWACCESS. ERA5 data (Bell et al., 2020; Hersbach et al., 2019) were downloaded from the Copernicus Climate Change Service (C3S) Climate Data Store. The ERA5 data are generated using Copernicus Climate Change Service information (2021). Neither the European Commission nor ECMWF is responsible for any use that may be made of the Copernicus information or data it contains. The MERRA-2 AOT used in this study has been provided by the Global Modeling and Assimilation Office (GMAO) at NASA Goddard Space Flight Center (Rienecker et al., 2011). The MERRA-2 data are freely available at the NASA Giovanni website: https://giovanni.gsfc.nasa.gov/giovanni/. The NASA AERONET AOT is freely available at https://aeronet.gsfc.nasa.gov/. In order to get access to energy flux measurements from the GEBA database (Wild et al., 2017), please use the following address: geba-contact@env.ethz.ch. Global Historical Climatology Network-Monthly (GHCN-M) version 4 data set of monthly mean temperatures was accessed from NOAA's National Centers for Environmental Information (NCEI) database (Lawrimore et al., 2011): https://www.ncei.noaa.gov/products/land-based-station/global-historical-climatology-network-monthly.

Acknowledgments
We thank the AERONET principal investigators and their staff for establishing and maintaining the AERONET sites used in this investigation. The Global Energy Balance Archive (GEBA) is cofunded by the Federal Office of Meteorology and Climatology Meteo Swiss within the framework of GCOS Switzerland. The work was financed through research grants from the Swedish Research Council for the Environment, Agricultural Sciences and Spatial Planning (FORMAS). We would like to thank the three reviewers for their thoughtful comments and efforts toward improving the manuscript.

References

Acosta Navarro, J. A., Varma, V., Riipinen, I., Seland, Ø., Kirkevåg, A., Struthers, H., et al. (2016). Amplification of Arctic warming by past air pollution reductions in Europe. *Nature Geoscience*, *9*(4), 277–281. https://doi.org/10.1038/ngeo2673

Ångström, A. (1929). On the atmospheric transmission of sun radiation and on dust in the air. *Geografiska Annaler*, *11*(2), 156–166.

Archer, C. L., & Caldeira, K. (2008). Historical trends in the jet streams. *Geophysical Research Letters*, *35*, L08803. https://doi.org/10.1029/2008GL033614

Bell, B., Hersbach, H., Berrisford, P., Dahlgren, P., Horányi, A., Sabater, J. M., et al. (2020). ERA5 monthly averaged data on single levels from 1950 to 1978 (preliminary version) [Dataset]. Climate Data Store (CDS). Retrieved from https://cds.climate.copernicus-climate.eu/cdsapp#!/dataset/reanalysis-era5-single-levels-monthly-means-preliminary-back-extension?tab=overview

Blanc, A., Blanchet, J., & Creutin, J.-D. (2022). Past evolution and recent changes in Western Europe large-scale circulation. *Weather and Climate Dynamics*, *3*, 23–1250. https://doi.org/10.5194/wcd-3-231-2022

Boucher, O., & Haywood, J. (2001). On summing the components of radiative forcing of climate change. *Climate Dynamics*, *18*(3–4), 297–302. https://doi.org/10.1007/s003820100185

Boucher, O., Randall, D., Artaxo, P., Bretherton, C., Feingold, G., Forster, P., et al. (2013). Clouds and aerosols, climate change 2013: The physical science basis. In *Contribution of Working Group I to the Fifth Assessment Report of the Intergovernmental Panel on Climate Change* (pp. 571–657). Cambridge University Press.

Buchard, V., Randles, C., Da Silva, A., Darmenov, A., Colarco, P., Govindaraju, R., et al. (2017). The MERRA-2 aerosol reanalysis, 1980 onward. Part II: Evaluation and case studies. *Journal of Climate*, *30*(17), 6851–6872. https://doi.org/10.1175/JCLI-D-16-0613.1

Christensen, J. H., Kanikicharla, K. K., Aldrian, E., An, S. I., Cavalcanti, I. F. A., de Castro, M., et al. (2013). Climate phenomena and their relevance for future regional climate change. In *Climate change 2013 the physical science basis: Working Group I contribution to the Fifth Assessment Report of the Intergovernmental Panel on Climate Change* (pp. 1217–1308). Cambridge University Press.

Christidis, N., & Stott, P. A. (2021). The influence of anthropogenic climate change on wet and dry summers in Europe. *Science Bulletin*, *66*(8), 813–823. https://doi.org/10.1016/j.scib.2021.01.020

Cohen, J., Screen, J. A., Furtado, J. C., Barlow, M., Whittleston, D., Coumou, D., et al. (2014). Recent Arctic amplification and extreme mid-latitude weather. *Nature Geoscience*, *7*(9), 627–637. https://doi.org/10.1038/ngeo2234

Dee, D., Balmaseda, M., Balsamo, G., Engelen, R., Simmons, A., & Thépaut, J.-N. (2014). Toward a consistent reanalysis of the climate system. *Bulletin of the American Meteorological Society*, *95*(8), 1235–1248. https://doi.org/10.1175/BAMS-D-13-00043.1

De Meij, A., Pozzer, A., & Lelieveld, J. (2012). Trend analysis in aerosol optical depths and pollutant emission estimates between 2000 and 2009. *Atmospheric Environment*, *51*, 75–85. https://doi.org/10.1016/j.atmosenv.2012.01.059

Dong, B., Sutton, R. T., & Shaffrey, L. (2017). Understanding the rapid summer warming and changes in temperature extremes since the mid-1990s over Western Europe. *Climate Dynamics*, *48*(5–6), 1537–1554. https://doi.org/10.1007/s00382-016-3158-8

Eck, T., Holben, B., Reid, J., Dubovik, O., Smirnov, A., O'Neill, N., et al. (1999). Wavelength dependence of the optical depth of biomass burning, urban, and desert dust aerosols. *Journal of Geophysical Research*, *104*(D24), 31333–31349. https://doi.org/10.1029/1999JD900923

Fu, Q., Johanson, C. M., Wallace, J. M., & Reichler, T. (2006). Enhanced mid-latitude tropospheric warming in satellite measurements. *Science*, *312*(5777), 1179. https://doi.org/10.1126/science.1125566

Gago, J., Cabanas, J., Casas, G., & Miranda, A. (2011). Thermohaline measurements in the continental shelf zone of the NW Iberian Peninsula, 1994–2006. *Climate Research*, *48*(2–3), 219–229. https://doi.org/10.3354/cr00943

Giorgi, F. (2006). Climate change hot-spots. *Geophysical Research Letters*, *33*, L08707. https://doi.org/10.1029/2006GL025734

Glantz, P., Freud, E., Johansson, C., Noone, K. J., & Tesche, M. (2019). Trends in MODIS and AERONET derived aerosol optical thickness over Northern Europe. *Tellus B: Chemical and Physical Meteorology*, *71*(1), 1554414. https://doi.org/10.1080/16000889.2018.1554414

Granier, C., Bessagnet, B., Bond, T., D'Angiola, A., vanDer Gon, H. D., Frost, G. J., et al. (2011). Evolution of anthropogenic and biomass burning emissions of air pollutants at global and regional scales during the 1980–2010 period. *Climatic Change*, *109*(1), 163–190. https://doi.org/10.1007/s10584-011-0154-1

Hand, J., Schichtel, B., Malm, W., & Pitchford, M. (2012). Particulate sulfate ion concentration and SO_2 emission trends in the United States from the early 1990s through 2010. *Atmospheric Chemistry and Physics*, *12*(21), 10353–10365. https://doi.org/10.5194/acp-12-10353-2012

Hersbach, H., Bell, B., Berrisford, P., Biavati, G., Horányi, A., Muñoz Sabater, J., et al. (2019). ERA5 monthly averaged data on single levels from 1959 to present [Dataset]. Copernicus Climate Change Service (C3S) Climate Data Store (CDS). Retrieved from https://cds.climate.copernicus.eu/cdsapp#!/dataset/reanalysis-era5-single-levels-monthly-means?tab=form

Hersbach, H., Peubey, C., Simmons, A., Berrisford, P., Poli, P., & Dee, D. (2015). ERA-20CM: A twentieth-century atmospheric model ensemble. *Quarterly Journal of the Royal Meteorological Society*, *141*(691), 2350–2375. https://doi.org/10.1002/qj.2528

Holben, B., Eck, T., Slutsker, I., Tanre, D., Buis, J., Setzer, A., et al. (1998). AERONET—A federated instrument network and data archive for aerosol characterization. *Remote Sensing of Environment*, *66*(1), 1–16. https://doi.org/10.1016/s0034-4257(98)00031-5

Hu, Y., Huang, H., & Zhou, C. (2018). Widening and weakening of the Hadley circulation under global warming. *Science Bulletin*, *63*(10), 640–644. https://doi.org/10.1016/j.scib.2018.04.020

Hu, Y., Tao, L., & Liu, J. (2013). Poleward expansion of the Hadley circulation in CMIP5 simulations. *Advances in Atmospheric Sciences*, *30*(3), 790–795. https://doi.org/10.1007/s00376-012-2187-4

IPCC. (2013). Climate change 2013: The physical science basis. In T. F. Stocker, et al. (Eds.), *Contribution of Working Group I to the Fifth Assessment Report of the Intergovernmental Panel on Climate Change*. Cambridge University Press.

IPCC. (2014). Climate change 2014: Synthesis report. In *Contribution of Working Groups I, II and III to the Fifth Assessment Report of the Intergovernmental Panel on Climate Change*. IPCC.

IPCC. (2021). Climate change 2021: The physical science basis. In V. Masson-Delmotte, et al. (Eds.), *Contribution of Working Group I to the Sixth Assessment Report of the Intergovernmental Panel on Climate Change*. Cambridge University Press.

IPCC. (2022). *Global warming of 1.5°C: IPCC Special Report on impacts of global warming of 1.5°C above pre-industrial levels in context of strengthening response to climate change, sustainable development, and efforts to eradicate poverty*. Cambridge University Press.

Johannsen, F., Ermida, S., Martins, J., Trigo, I. F., Nogueira, M., & Dutra, E. (2019). Cold bias of ERA5 summertime daily maximum land surface temperature over Iberian Peninsula. *Remote Sensing*, *11*(21), 2570. https://doi.org/10.3390/rs11212570

Johanson, C. M., & Fu, Q. (2009). Hadley cell widening: Model simulations versus observations. *Journal of Climate*, *22*(10), 2713–2725. https://doi.org/10.1175/2008JCLI2620.1

Jong, R. D., & Stewart, D. (1993). Estimating global solar radiation from common meteorological observations in Western Canada. *Canadian Journal of Plant Science*, *73*(2), 509–518. https://doi.org/10.4141/cjps93-068

Kaufman, Y., Koren, I., Remer, L., Tanré, D., Ginoux, P., & Fan, S. (2005). Dust transport and deposition observed from the Terra-Moderate resolution Imaging Spectroradiometer (MODIS) spacecraft over the Atlantic Ocean. *Journal of Geophysical Research*, *110*), D10S12. https://doi.org/10.1029/2003JD004436

Kim, D., & Ramanathan, V. (2008). Solar radiation budget and radiative forcing due to aerosols and clouds. *Journal of Geophysical Research*, *113*, D02203. https://doi.org/10.1029/2007JD008434

Kishcha, P., Starobinets, B., & Alpert, P. (2007). Latitudinal variations of cloud and aerosol optical thickness trends based on MODIS satellite data. *Geophysical Research Letters*, *34*, L05810. https://doi.org/10.1029/2006GL028796

Lamarque, J.-F., Bond, T. C., Eyring, V., Granier, C., Heil, A., Klimont, Z., et al. (2010). Historical (1850–2000) gridded anthropogenic and biomass burning emissions of reactive gases and aerosols: Methodology and application. *Atmospheric Chemistry and Physics*, *10*(15), 7017–7039. https://doi.org/10.5194/acp-10-7017-2010

Lashof, D. A., & Ahuja, D. R. (1990). Relative contributions of greenhouse gas emissions to global warming. *Nature*, *344*(6266), 529–531. https://doi.org/10.1038/344529a0

Lawrimore, J. H., Menne, M. J., Gleason, B. E., Williams, C. N., Wuertz, D. B., Vose, R. S., & Rennie, J. (2011). An overview of the Global Historical Climatology Network monthly mean temperature data set, version 3. *Journal of Geophysical Research*, *116*), D19121. https://doi.org/10.1029/2011JD016187

Liepert, B. G. (2002). Observed reductions of surface solar radiation at sites in the United States and worldwide from 1961 to 1990. *Geophysical Research Letters*, *29*(10), 1421. https://doi.org/10.1029/2002GL014910

Liou, K.-N. (2002). *An introduction to atmospheric radiation*. Elsevier.

Lorenz, R., Stalhandske, Z., & Fischer, E. M. (2019). Detection of a climate change signal in extreme heat, heat stress, and cold in Europe from observations. *Geophysical Research Letters*, *46*, 8363–8374. https://doi.org/10.1029/2019GL082062

Luo, Z., Yang, J., Gao, M., & Chen, D. (2020). Extreme hot days over three global mega-regions: Historical fidelity and future projection. *Atmospheric Science Letters*, *21*, e1003. https://doi.org/10.1002/asl.1003

Mateos, D., Sanchez-Lorenzo, A., Antón, M., Cachorro, V., Calbó, J., Costa, M. J., et al. (2014). Quantifying the respective roles of aerosols and clouds in the strong brightening since the early 2000s over the Iberian Peninsula. *Journal of Geophysical Research: Atmospheres*, *119*, 10382–10393. https://doi.org/10.1002/2014JD022076

Maturilli, M., Herber, A., & König-Langlo, G. (2014). Surface radiation climatology for Ny-Ålesund, Svalbard (78.9 N), basic observations for trend detection. *Theoretical and Applied Climatology*, *120*(1), 331–339. https://doi.org/10.1007/s00704-014-1173-4

Mortier, A., Gliß, J., Schulz, M., Aas, W., Andrews, E., Bian, H., et al. (2020). Evaluation of climate model aerosol trends with ground-based observations over the last 2 decades—An AeroCom and CMIP6 analysis. *Atmospheric Chemistry and Physics*, *20*(21), 13355–13378. https://doi.org/10.5194/acp-20-13355-2020

Nabat, P., Somot, S., Mallet, M., Sanchez-Lorenzo, A., & Wild, M. (2014). Contribution of anthropogenic sulfate aerosols to the changing Euro-Mediterranean climate since 1980. *Geophysical Research Letters*, *41*, 5605–5611. https://doi.org/10.1002/2014GL060798

Pinker, R., Zhang, B., & Dutton, E. (2005). Do satellites detect trends in surface solar radiation? *Science*, *308*(5723), 850–854. https://doi.org/10.1126/science.1103159

Ramanathan, V., Crutzen, P., Kiehl, J., & Rosenfeld, D. (2001). Aerosols, climate, and the hydrological cycle. *Science*, *294*(5549), 2119–2124. https://doi.org/10.1126/science.1064034

Randles, C., Da Silva, A., Buchard, V., Colarco, P., Darmenov, A., Govindaraju, R., et al. (2017). The MERRA-2 aerosol reanalysis, 1980 onward. Part I: System description and data assimilation evaluation. *Journal of Climate*, *30*(17), 6823–6850. https://doi.org/10.1175/JCLI-D-16-0609.1

Ricchiazzi, P., Yang, S., Gautier, C., & Sowle, D. (1998). SBDART: A research and teaching software tool for plane-parallel radiative transfer in the Earth's atmosphere. *Bulletin of the American Meteorological Society*, *79*(10), 2101–2114. https://doi.org/10.1175/1520-0477(1998)079<2101:SARATS>2.0.CO;2

Rienecker, M. M., Suarez, M. J., Gelaro, R., Todling, R., Bacmeister, J., Liu, E., et al. (2011). MERRA: NASA's Modern-Era Retrospective analysis for Research and Applications. *Journal of Climate*, *24*(14), 3624–3648. https://doi.org/10.1175/JCLI-D-11-00015.1

Sanchez-Lorenzo, A., Calbó, J., & Wild, M. (2013). Global and diffuse solar radiation in Spain: Building a homogeneous dataset and assessing their trends. *Global and Planetary Change*, *100*, 343–352. https://doi.org/10.1016/j.gloplacha.2012.11.010

Seidel, D. J., Fu, Q., Randel, W. J., & Reichler, T. J. (2008). Widening of the tropical belt in a changing climate. *Nature Geoscience*, *1*(1), 21–24. https://doi.org/10.1038/ngeo.2007.38

Seinfeld, J. H., & Pandis, S. N. (2016). *Atmospheric chemistry and physics: From air pollution to climate change*. John Wiley & Sons.

Serreze, M. C., & Barry, R. G. (2011). Processes and impacts of Arctic amplification: A research synthesis. *Global and Planetary Change*, *77*(1–2), 85–96. https://doi.org/10.1016/j.gloplacha.2011.03.004

Sfică, L., Beck, C., Nita, A. I., Voiculescu, M., Birsan, M. V., & Philipp, A. (2020). Cloud cover changes driven by atmospheric circulation in Europe during the last decades. *International Journal of Climatology*, *41*, E2211–E2230.

Smirnov, A., Holben, B., Eck, T., Dubovik, O., & Slutsker, I. (2000). Cloud-screening and quality control algorithms for the AERONET database. *Remote Sensing of Environment*, *73*(3), 337–349. https://doi.org/10.1016/s0034-4257(00)00109-7

Smith, S. J., van Aardenne, J., Klimont, Z., Andres, R. J., Volke, A., & Delgado Arias, S. (2011). Anthropogenic sulfur dioxide emissions: 1850–2005. *Atmospheric Chemistry and Physics*, *11*(3), 1101–1116. https://doi.org/10.5194/acp-11-1101-2011

Stanhill, G., & Cohen, S. (2001). Global dimming: A review of the evidence for a widespread and significant reduction in global radiation with discussion of its probable causes and possible agricultural consequences. *Agricultural and Forest Meteorology*, *107*(4), 255–278. https://doi.org/10.1016/s0168-1923(00)00241-0

Svensen, H., Planke, S., Chevallier, L., Malthe-Sørenssen, A., Corfu, F., & Jamtveit, B. (2007). Hydrothermal venting of greenhouse gases triggering Early Jurassic global warming. *Earth and Planetary Science Letters*, *256*(3–4), 554–566. https://doi.org/10.1016/j.epsl.2007.02.013

Szopa, S., Naik, V., Adhikary, B., Artaxo, P., Berntsen, T., Collins, W. D., et al. (2021). Short-lived climate forcers. In V.Masson-Delmotte, et al. (Eds.), *Climate change 2021: The physical science basis. Contribution of Working Group I to the Sixth Assessment Report of the Intergovernmental Panel on Climate Change* (pp. 817–922). Cambridge University Press. https://doi.org/10.1017/9781009157896.008

Tao, M., Wang, L., Chen, L., Wang, Z., & Tao, J. (2020). Reversal of aerosol properties in Eastern China with rapid decline of anthropogenic emissions. *Remote Sensing*, *12*(3), 523. https://doi.org/10.3390/rs12030523

Tegen, I., Hollrig, P., Chin, M., Fung, I., Jacob, D., & Penner, J. (1997). Contribution of different aerosol species to the global aerosol extinction optical thickness: Estimates from model results. *Journal of Geophysical Research*, *102*(D20), 23895–23915. https://doi.org/10.1029/97JD01864

Tuel, A., & Eltahir, E. A. (2021). Mechanisms of European summer drying under climate change. *Journal of Climate*, *34*(22), 8913–8931. https://doi.org/10.1175/JCLI-D-20-0968.1

Tunved, P., & Ström, J. (2019). On the seasonal variation in observed size distributions in northern Europe and their changes with decreasing anthropogenic emissions in Europe: Climatology and trend analysis based on 17 years of data from Aspvreten, Sweden. *Atmospheric Chemistry and Physics*, *19*(23), 14849–14873. https://doi.org/10.5194/acp-19-14849-2019

Turnock, S., Butt, E., Richardson, T., Mann, G., Reddington, C., Forster, P., et al. (2016). The impact of European legislative and technology measures to reduce air pollutants on air quality, human health and climate. *Environmental Research Letters*, *11*(2), 024010. https://doi.org/10.1088/1748-9326/11/2/024010

Turnock, S., Spracklen, D., Carslaw, K., Mann, G., Woodhouse, M., Forster, P., et al. (2015). Modelled and observed changes in aerosols and surface solar radiation over Europe between 1960 and 2009. *Atmospheric Chemistry and Physics*, *15*(16), 9477–9500. https://doi.org/10.5194/acp-15-9477-2015

Undorf, S., Bollasina, M., & Hegerl, G. (2018). Impacts of the 1900–74 increase in anthropogenic aerosol emissions from North America and Europe on Eurasian summer climate. *Journal of Climate*, *31*(20), 8381–8399. https://doi.org/10.1175/JCLI-D-17-0850.1

Vanden Besselaar, E. J., Sanchez-Lorenzo, A., Wild, M., Klein Tank, A. M., & De Laat, A. (2015). Relationship between sunshine duration and temperature trends across Europe since the second half of the twentieth century. *Journal of Geophysical Research: Atmospheres*, *120*, 10823–10836. https://doi.org/10.1002/2015JD023640

Vestreng, V., Myhre, G., Fagerli, H., Reis, S., & Tarrasón, L. (2007). Twenty-five years of continuous sulphur dioxide emission reduction in Europe. *Atmospheric Chemistry and Physics*, *7*, 3663–3681. https://doi.org/10.5194/acp-7-3663-2007

von Hoyningen-Huene, W., Joon, Y., Vountas, M., Istomina, G., Rohen, G., Dinter, T., et al. (2011). Retrieval of spectral aerosol optical thickness over land using ocean color sensors MERIS and SeaWiFS. *Atmospheric Measurement Technique*, *4*(4), 151–171. https://doi.org/10.5194/amt-4-151-2011

Wang, Y., Meng, Z., Lyu, R., Huang, G., He, Q., & Cheng, T. (2020). Spatiotemporal changes of surface solar radiation: Implication for air pollution and rice yield in East China. *Science of the Total Environment*, *739*, 140361.

Wang, Y., & Yang, Y. (2014). China's dimming and brightening: Evidence, causes and hydrological implications. *Annales Geophysicae*, *32*(1), 41–55. https://doi.org/10.5194/angeo-32-41-2014

Wild, M. (2009). Global dimming and brightening: A review. *Journal of Geophysical Research*, *114*, D00D16. https://doi.org/10.1029/2008JD011470

Wild, M., Gilgen, H., Roesch, A., Ohmura, A., Long, C. N., Dutton, E. G., et al. (2005). From dimming to brightening: Decadal changes in solar radiation at Earth's surface. *Science*, *308*(5723), 847–850. https://doi.org/10.1126/science.1103215

Wild, M., Ohmura, A., Schär, C., Müller, G., Folini, D., Schwarz, M., et al. (2017). The Global Energy Balance Archive (GEBA) version 2017: A database for worldwide measured surface energy fluxes. *Earth System Science Data*, *9*(2), 601–613. https://doi.org/10.5194/essd-9-601-2017

Wild, M., Wacker, S., Yang, S., & Sanchez-Lorenzo, A. (2021). Evidence for clear-sky dimming and brightening in Central Europe. *Geophysical Research Letters*, *48*, e2020GL092216. https://doi.org/10.1029/2020GL092216

Xia, X., Wang, P., Chen, H., & Liang, F. (2006). Analysis of downwelling surface solar radiation in China from National Centers for Environmental Prediction reanalysis, satellite estimates, and surface observations. *Journal of Geophysical Research*, *111*, D09103. https://doi.org/10.1029/2005JD006405

Yang, H., Lohmann, G., Lu, J., Gowan, E. J., Shi, X., Liu, J., & Wang, Q. (2020). Tropical expansion driven by poleward advancing midlatitude meridional temperature gradients. *Journal of Geophysical Research: Atmospheres*, *125*, e2020JD033158. https://doi.org/10.1029/2020JD033158

Yang, Y., Lou, S., Wang, H., Wang, P., & Liao, H. (2020). Trends and source apportionment of aerosols in Europe during 1980–2018. *Atmospheric Chemistry and Physics*, *20*(4), 2579–2590. https://doi.org/10.5194/acp-20-2579-2020

Yi, B., Yang, P., Bowman, K. P., & Liu, X. (2012). Aerosol–cloud–precipitation relationships from satellite observations and global climate model simulations. *Journal of Applied Remote Sensing*, *6*(1), 063503.